

ISSN: 2349-6495(P) | 2456-1908 (O)



International Journal of Advanced Engineering Research and Science

(IJAERS)

An Open Access Peer-Reviewed International Journal



Journal DOI: 10.22161/ijaers

Issue DOI: 10.22161/ijaers.119

AI PUBLICATIONS

Vol.- 11 | Issue - 9 | Sep 2024

editor.ijaers@gmail.com | editor@ijaers.com | <https://www.ijaers.com/>

International Journal of Advanced Engineering Research and Science (IJAERS)

(ISSN: 2349-6495(P)| 2456-1908(O))

DOI: 10.22161/ijaers

Vol-11, Issue-9

September, 2024

Editor in Chief

Dr. Swapnesh Taterh

Chief Executive Editor

S. Suman Rajest

Copyright © 2024 International Journal of Advanced Engineering Research and Science

Publisher

AI Publication

Email: editor.ijaers@gmail.com; editor@ijaers.com

Web: www.ijaers.com

International Editorial/ Reviewer Board

Editor in Chief

- **Dr. Swapnesh Taterh (Chief-Editor)**, Amity University, Jaipur, India

Chief Executive Editor

- **S. Suman Rajest**, Vels Institute of Science, Technology & Advanced Studies, India
chief-executive-editor@ijaers.com

Associate Editors

- **Dr. Ram Karan Singh**, King Khalid University, Guraiger, Abha 62529, Saudi Arabia
- **Dr. Shuai Li**, University of Cambridge, England, Great Britain

Editorial Member

- **Behrouz Takabi**, PhD, Texas A&M University, Texas, USA
- **Dr. Gamal Abd El-Nasser Ahmed Mohamed Said**, Port Training Institute (PTI), Arab Academy For Science, Technology and Maritime Transport, Egypt
- **Dr. Hou, Cheng-I**, Chung Hua University, Hsinchu Taiwan
- **Dr. Ebrahim Nohani**, Islamic Azad University, Dezful, IRAN.
- **Dr. Ahmadad Nabih Zaki Rashed**, Menoufia University, EGYPT
- **Dr. Rabindra Kayastha**, Kathmandu University, Nepal
- **Dr. Dinh Tran Ngoc Huy**, Banking and Finance, HCM, Viet Nam
- **Dr. Engin NAS**, Duzce University, Turkey
- **Dr. A. Heidari**, California South University (CSU), Irvine, California, USA
- **Dr. Uma Choudhary**, Mody University, Lakshmangarh, India
- **Dr. Varun Gupta**, National Informatic Center, Delhi, India
- **Dr. Ahmed Kadhim Hussein**, University of Babylon, Republic of Iraq
- **Dr. Vibhash Yadav**, Rajkiya Engineering College, Banda. UP, India
- **Dr. M. Kannan**, SCSVMV University, Kanchipuram, Tamil Nadu, India
- **José G. Vargas-Hernández**, University of Guadalajara Periférico Norte 799 Edif. G201-7, Núcleo Universitario Los Belenes, Zapopan, Jalisco, 45100, México
- **Dr. Sambit Kumar Mishra**, Gandhi Institute for Education and Technology, Baniatangi, Bhubaneswar, India
- **DR. C. M. Velu**, Datta Kala Group of Institutions, Pune, India
- **Dr. Deependra Pandey**, Amity University, Uttar Pradesh, India
- **Dr. K Ashok Reddy**, MLR Institute of Technology, Dundigal, Hyderabad, India
- **Dr. S.R.Boselin Prabhu**, SVS College of Engineering, Coimbatore, India
- **N. Balakumar**, Tamilnadu College of Engineering, Karumathampatti, Coimbatore, India
- **R. Poorvadevi**, SCSVMV University, Enathur, Kanchipuram, Tamil Nadu, India
- **Dr. Subha Ganguly**, Arawali Veterinary College, Sikar, India
- **Dr. P. Murali Krishna Prasad**, GVP College of Engineering for Women, Visakhapatnam, Andhra Pradesh, India
- **Anshul Singhal**, Bio Instrumentation Lab, MIT, USA
- **Mr. Lusekelo Kibona**, Ruaha Catholic University, Iringa, Tanzania
- **Sina Mahdavi**, Urmia Graduate Institute, Urmia, Iran
- **Dr. N. S. Mohan**, Manipal Institute of Technology, Manipal, India
- **Dr. Zafer Omer Ozdemir**, University of Health Sciences, Haydarpassa, Uskudar, Istanbul, TURKIYE
- **Bingxu Wang**, 2721 Patrick Henry St Apt 510, Auburn Hills, Michigan, United States

- **Dr. Jayashree Patil-Dake**, KPB Hinduja College of Commerce, Mumbai, India
- **Dr. Neel Kamal Purohit**, S.S. Jain Subodh P.G. College, Rambagh, Jaipur, India
- **Mohd Muntjir**, Taif University, Kingdom of Saudi Arabia
- **Xian Ming Meng**, China Automotive Technology & Research Center No.68, East Xianfeng Road, Dongli District, Tianjin, China
- **Herlandi de Souza Andrade**, FATEC Guaratingueta, State Center for Technological Education Paula Souza - CEETEPS
- **Dr. Payal Chadha**, University of Maryland University College Europe, Kuwait
- **Ahmed Moustafa Abd El-hamid Elmahalawy**, Menoufia University, Al Minufya, Egypt
- **Prof. Mark H. Rummeli**, University & Head of the characterisation center, Soochow Institute for Energy Materials Innovations (SIEMES), Suzhou, Jiangsu Province, China
- **Dr. Eman Yaser Daraghmi**, Ptuk, Tulkarm, Palestine
- **Holmes Rajagukguk**, State University of Medan, Lecturer in Sisingamangaraja University North Tapanuli, Indonesia
- **Dr. Menderes KAM**, Dr. Engin PAK Cumayeri Vocational School, DÜZCE UNIVERSITY (University in Turkey), Turkey
- **Dr. Jatin Goyal**, Punjabi University, Patiala, Punjab, India | International Collaborator of GEITEC / UNIR / CNPq, Brazil
- **Ahmet İPEKÇİ**, Dr. Engin PAK Cumayeri Vocational School, DÜZCE UNIVERSITY, Turkey
- **Baarimah Abdullah Omar**, Universiti Malaysia Pahang (UMP), Gambang, 26300, Malaysia
- **Sabri UZUNER**, Dr. Engin PAK Cumayeri Vocational School Cumayeri/Duzce/Turkey
- **Ümit AĞBULUT**, Düzce University, Turkey
- **Dr. Mustafa ÖZKAN**, Trakya University, Edirne/ TURKEY
- **Dr. Indrani Bhattacharyya**, Dr. B.C. Roy College of Pharmacy and Allied Health Sciences, Durgapur, West Bengal, India
- **Egnon Kouakou**, Nutrition/Health at University Felix Houphouet Boigny Abidjan, Ivory Coast
- **Dr. Suat SARIDEMİR**, Düzce University, Faculty of Technology, Turkey
- **Dr. Manvinder Singh Pahwa**, Director, Alumni Relations at Manipal University Jaipur, India
- **Omid Habibzadeh Bigdarvish**, University of Texas at Arlington, Texas, USA
- **Professor Dr. Ho Soon Min**, INTI International University, Jln BBN 12/1, Bandar, Baru Nilai, 71800 Negeri Sembilan, Malaysia
- **Ahmed Mohammed Morsy Hassan**, South Egypt Cancer Institute, Assiut University, Assiut, Egypt
- **Xian Ming Meng (Ph.D)**, China Automotive Technology & Research Center, No.68, East Xianfeng Road, Tianjin, China
- **Ömer Erkan**, Konuralp Campus, Düzce-Turkey
- **Dr. Yousef Daradkeh**, Prince Sattam bin Abdulaziz University) PSAU), KSA
- **Peter JO**, IPB University, Indonesia
- **Nazmi Liana Binti Azmi**, Raja Perempuan Zainab II Hospital, 15586 Kota Bharu, Kelantan, Malaysia
- **Mr. Sagar Jamle**, Oriental University, Indore, India
- **Professor Grazione de Souza**, Applied Mathematics, Rio de Janeiro State University, Brazil
- **Kim Edward S. Santos**, Nueva Ecija University of Science and Technology, Philippines.

Vol-11, Issue-9, September 2024
(10.22161/ijaers.119)

Detail with DOI (CrossRef)

Comparative analysis of Chlorophyll concentration in different species of leafy vegetables cultivated in soil and hydroponic system

Ghritlahre R, Prabhas L., Megha A.

 DOI: [10.22161/ijaers.119.1](https://doi.org/10.22161/ijaers.119.1)

Page No: 01-06

The Relationship Between Wave Period, Deep Water Wave and Breaking Wave Heights, Formulated Using the Wave Amplitude Function

Syawaluddin Hutahaean

 DOI: [10.22161/ijaers.119.2](https://doi.org/10.22161/ijaers.119.2)

Page No: 07-15

Research on heat transfer model prediction of Tesla Valve heat sink based on training neural network method

Yan-Xiao Jia, Yan-Zuo Chang, Guo-Xing Yang, Ruo-Yu Yang, Yi-wei Zhang, Ting-Hao Zhang

 DOI: [10.22161/ijaers.119.3](https://doi.org/10.22161/ijaers.119.3)

Page No: 16-25

Afro-Womanism and the Development of Gender Consciousness

Dr Ibrahim Yekini, Armande M. Hounkpe

 DOI: [10.22161/ijaers.119.4](https://doi.org/10.22161/ijaers.119.4)

Page No: 26-32

Simulation Study on Heat Transfer Conditions Based on Vertically Descending Evaporating Tubes

Guo-Xing Yang, Yan-Zuo Chang, Yan-Xiao Jia, Jin-Ping Chen, Shao-Bi Dai, Yu-Qiang Lin

 DOI: [10.22161/ijaers.119.5](https://doi.org/10.22161/ijaers.119.5)

Page No: 33-42

Comparative analysis of Chlorophyll concentration in different species of leafy vegetables cultivated in soil and hydroponic system

Ghritlahre R, Prabhas* L., Megha A.

¹M.Sc. Bioscience, PRSU, Raipur, Chhattisgarh, India

^{2*}Assistant Professor in Bioscience, PRSU, Raipur, Chhattisgarh, India

³Assistant Professor, Dept. of Botany, Gurukul Mahila Mahavidyalaya, Kalibadi Raipur

e-mail: labya_127@yahoo.co.in

Received: 25 Jul 2024,

Receive in revised form: 26 Aug 2024,

Accepted: 04 Sep 2024,

Available online: 10 Sep 2024

©2024 The Author(s). Published by AI
Publication. This is an open-access article under
the CC BY license

(<https://creativecommons.org/licenses/by/4.0/>).

Keywords— Leafy vegetables, hydroponics,
chlorophyll, soil, system, amount.

Abstract— Leafy vegetables are an important vegetable crop that grows easily under controlled conditions, such as in hydroponic. A plant's leaf colours can be used to indicate stress levels due to its adaptability to environmental changes. In this study, the samples were cultivated in the backyard of the Life Science department in Pandit Ravishankar Shukla University, Raipur, Chhattisgarh during January to April 2024. In this study, fresh mature leaves of soil-cultivated plants and hydroponically cultivated plants were taken for chlorophyll estimation. The sample was tested using an acetone solution (80%) and the information from the spectrum was calculated using the Arnon's method. The levels of Chl. a and Chl. b in soil-grown and hydroponically grown plants have been found to differ. Hydroponic cultivated plants show a high amount of total chlorophyll content as compared to soil-based plants and the reason behind the high level of chlorophyll content in a hydroponic system is controlled environmental conditions that mean precise control over light, temperature, and nutrient availability and are highly specific from species to species whereas, in a soil-based system, it is difficult to maintain such condition.

I. INTRODUCTION

The chlorophyll contents in leafy vegetables have a considerable influence on their growth, as is commonly recognized. Chlorophyll concentration can be used to assess plant productivity and photosynthetic potential. The rate of photosynthesis in the plant is determined by the photosynthetic capacity per unit area of the leaf (Kozłowski *et al.* 1991), which is also shown by the chlorophyll concentration (Dickman & Kozłowski 1968). When it comes to leafy vegetables, color is an important component that influences consumer preferences and product quality assessment. Chlorophyll, the most common pigment in green plants, has become increasingly

important in the human diet. It serves as both a nutritious food ingredient and a natural food colorant (Xue, L., & Yang, L. 2009).

Chl. a and Chl. b are accessory pigments, and various other types of chlorophyll are present in leafy vegetables. The empirical formulas for Chl. a and Chl. b are $C_{55}H_{72}O_5N_4Mg$ and $C_{55}H_{70}O_6N_4Mg$, respectively. Typically, Chl. a appears blue-green, while Chl. b appears yellow-green (Witham & Devlin 1997). The developmental stage of the photosynthetic system in plants is also indicated by the chlorophyll a and b ratio. It plays a crucial part in the formation and growth of leafy vegetables. The amount of chlorophyll in leaf tissue is

influenced by nutrient availability and stresses such as drought, salinity, cold, heat, etc. However, nutrient availability and various stresses such as drought, salinity, cold, heat, etc. are factors that might also be responsible for color variation in eight different species of leafy vegetables. The present study was undertaken for a comparative analysis of chlorophyll concentration in soil-cultivated plants and hydroponic-cultivated plants in eight different species. *Raphanus sativus L.* (Mooli bhaji), *Chorchorus oltorius L.* (Chech bhaji), *Lathyrus sativus L.* (Lakhdi bhaji), *Carthamus tinctorius L.* (Kusum bhaji), *Amaranthus tricolor L.* (Lal bhaji), *Mentha piperital L.* (Peppermint), *Ipomea aquatica F.* (Karmata bhaji), and *Trigonella foenum-graecum L.* (Methi bhaji).

Literature reviewed and popularity of hydroponics is increasing day by day. Hydroponics uses dissolved nutrients in water, allowing plants to grow food closer to consumers. It produces superior quality, is not seasonal, and is environmentally friendly. Hydroponic systems, including nutrient film techniques, wick systems, and aeroponic systems, ensure plant production success. Hydroponic farming uses water, nutrients, and pest control to grow crops like lettuce, vegetables, herbs, and flowers. It saves 70-90% water, yields three times more, and uses 60% less fertilizer than traditional methods. Proper control is essential for environmental benefits.

II. MATERIAL AND METHODS

Eight different species of leafy vegetables namely *Raphanus sativus L.* (Mooli bhaji), *Chorchorus oltorius L.* (Chech bhaji), *Lathyrus sativus L.* (Lakhdi bhaji), *Carthamus tinctorius L.* (Kusum Bhaji), *Amaranthus tricolor L.* (Lal bhaji), *Mentha piperital L.* (Peppermint), *Ipomea aquatica F.* (Karmata bhaji), and *Trigonella*

foenum-graecum L. (Methi bhaji) were selected for the present study. The samples were cultivated in the backyard of the Life Science department in Pandit Ravishankar Shukla University, Raipur, Chhattisgarh (India) during January to April the year 2023-2024. In this experiment, fresh mature leaves of soil-cultivated plants and hydroponically cultivated plants were taken for chlorophyll estimation. One gram leaf from each species is measured and grounded using a mortar and pestle after being chopped into small bits. After that, 0.5 g of (MgCo3) powder and 20 ml of 80% acetone were added, and the mixture was carefully ground using the technique of (Kamble et al. 2015). After that, the mixture was incubated for three hours at 4°C. The mixture was centrifuged at 2500 rpm for 5 min and the supernatant was transferred to a 100 ml volumetric flask the volume was made up to 100ml with the addition of 80% acetone and the solution was used for chlorophyll estimation (Fig.1). The absorbance of solutions was measured at 645 nm and 663 nm in SYSTRONICS Spectrophotometer 106 taking the 80% acetone solution as blank (Sadasivam & Manickam 1996).The reading was taken in a triplicate sample and the average was considered for the calculation of chlorophyll content. The chlorophyll a, b, and a + b (total chlorophyll) contents were calculated by applying the following (Arnon 1949) formulae:-

$$\text{Chlorophyll a (mg /g tissue)} = \frac{12.7 (A_{663}) - 2.69 (A_{645}) \times V}{1000 \times W}$$

$$\text{Chlorophyll b (mg g-1 tissue)} = \frac{22.9 (A_{645}) - 4.68 (A_{663}) \times V}{1000 \times W}$$

$$\text{Total chlorophyll (mg g-1 tissue)} = \frac{20.2 (A_{645}) - 8.02 (A_{663}) \times V}{1000 \times W}$$

Where, A = absorbance at a specific wavelength

V = final volume of chlorophyll extract in 80% acetone

W = fresh weight of tissue extracted

III. RESULT AND DISSCUSION

Table 1. Chlorophyll concentration in eight different leafy vegetable species in soil.

S. No.	Name of leafy vegetables	O.D. Reading		Soil Cultivated Plants		
		645 nm	663 nm	Chl.a (mg g ⁻¹)	Chl.b (mg g ⁻¹)	Total Chl (mg g ⁻¹)
1	<i>Raphanus Sativus L.</i>	0.443 ± 0.001	0.202 ± 0.001	0.137	0.919	1.056
2	<i>Chorchorus trilocularis L.</i>	0.431 ± 0.0005	0.117 ± 0.003	0.0326	0.932	0.964
3	<i>Lathyrus sativus L.</i>	0.212 ± 0.0005	0.134 ± 0.0015	0.113	0.422	0.535
4	<i>Carthamus tinctorius L.</i>	0.379 ± 0.0015	0.106 ± 0.0015	0.0326	0.818	0.850
5	<i>Amaranthus tricolor L.</i>	0.256 ± 0.001	0.172 ± 0.0011	0.149	0.505	0.655
6	<i>Mentha arvensis</i>	0.418 ± 0.0005	0.109 ± 0.0005	0.0259	0.906	0.931
7	<i>Ipomea aquatica F.</i>	0.053 ± 0.0025	0.024 ± 0.001	0.0162	0.110	0.126
8	<i>Trigonellafoenum- graecum L.</i>	0.559 ± 0.001	0.140 ± 0.01	0.0274	1.21	1.241

Table 2. Chlorophyll concentration in eight different leafy vegetable species in hydroponics.

S. No.	Name of leafy vegetables	O.D. Reading		Hydroponic Cultivated Plants		
		645 nm	663 nm	Chl.a (mg g ⁻¹)	Chl.b (mg g ⁻¹)	Total Chl (mg g ⁻¹)
1	<i>Raphanus Sativus L.</i>	0.558 ± 0.002	0.138 ± 0.003	0.0251	1.213	1.237
2	<i>Chorchorus trilocularis L.</i>	0.773 ± 0.002	0.206 ± 0.002	0.0536	1.673	1.726
3	<i>Lathyrus sativus L.</i>	0.297 ± 0.012	0.139 ± 0.008	0.096	0.615	0.711
4	<i>Carthamus tinctorius L.</i>	1.205 ± 0.002	0.284 ± 0.005	0.0365	2.626	2.661
5	<i>Amaranthus tricolor L.</i>	0.613 ± 0.002	0.139 ± 0.001	0.0116	1.338	1.349
6	<i>Mentha arvensis</i>	0.689 ± 0.001	0.151 ± 0.002	0.006	1.507	1.512
7	<i>Ipomea aquatica F.</i>	0.517 ± 0.002	0.120 ± 0.005	0.0133	1.127	1.140
8	<i>Trigonellafoenum-graecum L.</i>	0.617 ± 0.003	0.195 ± 0.001	0.0816	1.321	1.402

The study revealed that the chlorophyll *Chl.*(a + b) in soil-cultivated plants ranges from 0.0162 to 0.149 mg g⁻¹ and in hydroponic-cultivated plants ranges from 0.006 to 0.096 mg g⁻¹, and *Chl. b* in soil-cultivated plants ranges from 0.110 to 1.21 mg g⁻¹ and in hydroponic-cultivated plants ranges from 0.615 to 2.626 mg g⁻¹. The total chlorophyll *Chl. (a + b)* in soil-cultivated plants ranges from 0.126 to 1.241 mg g⁻¹ and in hydroponic-cultivated plants ranges from 0.711 to 2.661 mg g⁻¹ in eight leafy vegetable species. From the above result, it is also seen that *Trigonella foenum-graecum L.* has the highest concentration of *Chl. a* and *Chl.b*. *Ipomea aquatica F.* has the lowest concentration of *Chl. a* and *Chl. b* among the eight species in soil-cultivated plants, whereas in hydroponic-cultivated plants, *Carthamus tinctorius L.* has the highest concentration of *Chl. a* and *Chl. b*. *Lathyrus sativus L.* has the lowest concentration of *Chl. a* and *Chl. b* among the eight species. The highest total chlorophyll content in the soil-cultivated plant is shown by *Trigonella foenum-graecum L.* (1.241 mg g⁻¹) whereas in hydroponics, *Carthamus tinctorius L.* (2.661 mg g⁻¹) shows the highest total chlorophyll content and The lowest total chlorophyll content in the soil-cultivated plant is shown by *Ipomea aquatica F* (0.126 mg g⁻¹) whereas in hydroponics, *Lathyrus sativus L.* (0.711 mg g⁻¹) shows the lowest total chlorophyll content.

Raphanus sativus L. The total chlorophyll content in the soil-based system is 1.056 mg g⁻¹, whereas in a hydroponic system, it is 1.237 mg g⁻¹, which is 0.181 mg g⁻¹ higher than the soil-base system. The chlorophyll content in the soil-based system is 0.137 mg g⁻¹, whereas in the hydroponic system it is only 0.0251 mg g⁻¹, which is 0.111 mg g⁻¹ less than the soil-based system. The *Chl. b* content in the soil-based system is 0.919 mg g⁻¹, whereas in the

hydroponic system, it is 1.213 mg g⁻¹, which is 0.294 mg g⁻¹, higher than the soil-base system.

Chorchorus olitoriusL. The total chlorophyll content in the soil-based system is 0.964 mg g⁻¹, whereas in a hydroponic system, it is 1.726 mg g⁻¹, which is 0.762 mg g⁻¹, higher than the soil-base system. The *Chl. a* content in the soil-based system is 0.0326 mg g⁻¹, whereas in the hydroponic system it is 0.0536 mg g⁻¹, which is 0.021 mg g⁻¹ higher than the soil-based system. The *Chl. b* content in the soil-based system is 0.932 mg g⁻¹, whereas in a hydroponic system, it is 1.673 mg g⁻¹, which is 0.741 mg g⁻¹ higher than the soil-base system.

Lathyrus sativum L. The total chlorophyll content in the soil-based system is 0.535 mg g⁻¹, whereas in a hydroponic system, it is 0.711 mg g⁻¹, which is 0.176 mg g⁻¹ higher than the soil-base system. The *Chl. a* content in the soil-based system is 0.13 mg g⁻¹, whereas in the hydroponic system it is only 0.096 mg g⁻¹, which is 0.017 mg g⁻¹ less than the soil-based system. The *Chl. b* content in the soil-based system is 0.442 mg g⁻¹, whereas in a hydroponic system, it is 0.615 mg g⁻¹, which is 0.173 mg g⁻¹, higher than the soil-base system.

Carthamus tinctorius L. The total chlorophyll content in the soil-based system is 0.850 mg g⁻¹, whereas in a hydroponic system, it is 2.661 mg g⁻¹, which is 1.811 mg g⁻¹, higher than the soil-base system. The *Chl. a* content in the soil-based system is 0.0326 mg g⁻¹, whereas in the hydroponic system it is only 0.0365 mg g⁻¹, which is 0.0039 mg g⁻¹ higher than the soil-based system. The *Chl. b* content in the soil-based system is 0.818 mg g⁻¹, whereas in a hydroponic system, it is 2.626 mg g⁻¹, which is 1.808 mg g⁻¹, higher than the soil-base system.

Amaranthus tricolor L. The total chlorophyll content in the soil-based system is 0.655 mg g⁻¹, whereas in a

hydroponic system, it is 1.349 mg g⁻¹, which is 0.694 mg g⁻¹ higher than the soil-base system. The Chl. a content in the soil-based system is 0.149 mg g⁻¹, whereas in the hydroponic system it is only 0.0116 mg g⁻¹, which is 0.1374 mg g⁻¹ less than the soil-based system. The Chl. b content in the soil-based system is 0.505 mg g⁻¹, whereas in a hydroponic system, it is 1.338 mg g⁻¹, which is 0.833 mg g⁻¹, higher than the soil-base system.

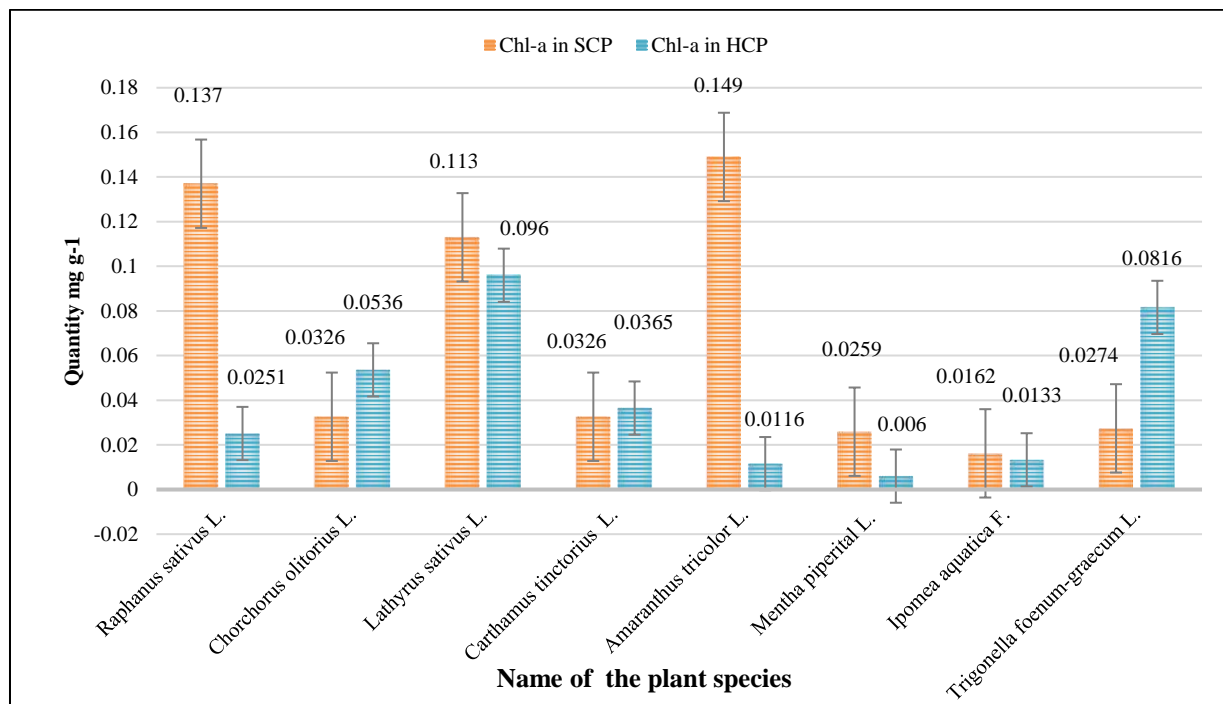
Mentha piperital L, The total chlorophyll content in the soil-based system is 0.931 mg g⁻¹, whereas in a hydroponic system, it is 1.512 mg g⁻¹, which is 0.581 mg g⁻¹, higher than the soil-base system. The Chl. a content in the soil-based system is 0.0259 mg g⁻¹, whereas in the hydroponic system it is only 0.006 mg g⁻¹, which is 0.0199 mg g⁻¹ less than the soil-based system. The Chl. b content in the soil-based system is 0.906 mg g⁻¹, whereas in a hydroponic system, it is 1.507 mg g⁻¹, which is 0.601 mg g⁻¹, higher than the soil-base system.

Ipomea aquatica F, The total chlorophyll content in the soil-based system is 0.126 mg g⁻¹, whereas in a hydroponic system, it is 1.140 mg g⁻¹, which is 1.014 mg g⁻¹, higher than the soil-base system. The Chl. a content in the soil-based system is 0.0162 mg g⁻¹, whereas in the hydroponic system it is only 0.0133 mg g⁻¹, which is 0.0029 mg g⁻¹ less than the soil-based system. The Chl. b content in the soil-based system is 0.110 mg g⁻¹, whereas in a hydroponic system, it is 1.127 mg g⁻¹, which is 1.017 mg g⁻¹, higher than the soil-base system.

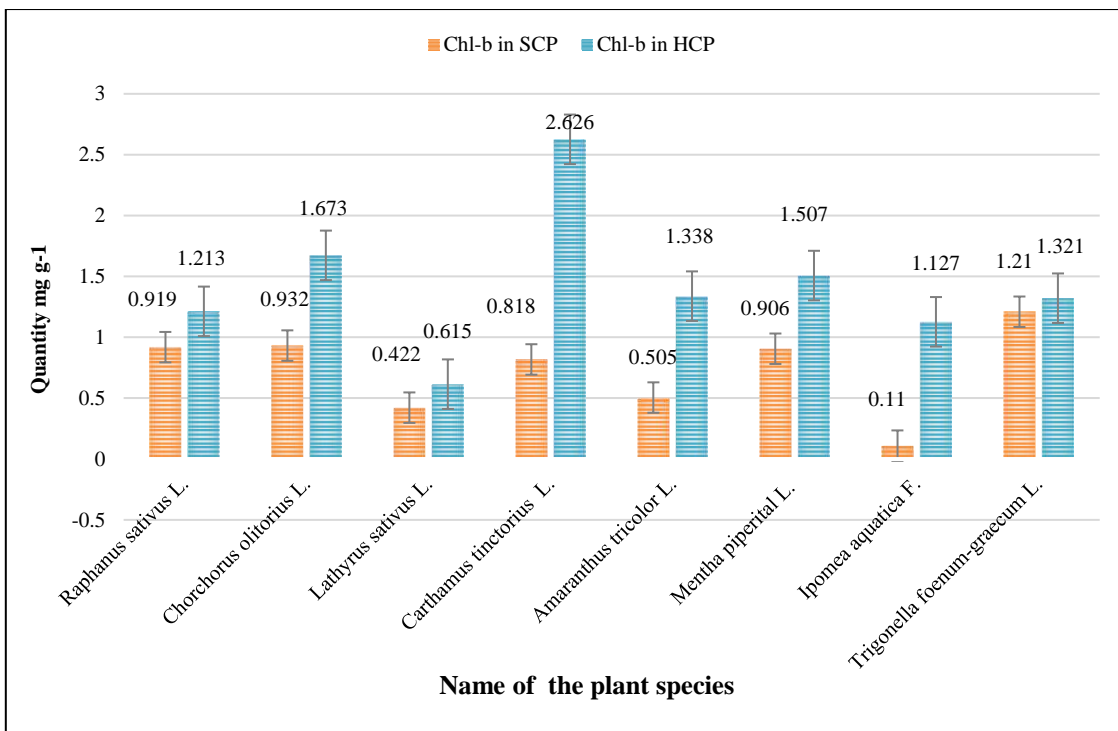
Trigonella foenum-graecum L, The total chlorophyll content in the soil-based system is 1.241 mg g⁻¹, whereas in a hydroponic system, it is 1.402 mg g⁻¹, which is 0.161 mg g⁻¹ higher than the soil-base system. The Chl. a content in the soil-based system is 0.0274 mg g⁻¹, whereas in the hydroponic system it is only 0.0133 mg g⁻¹, which is 0.0141 mg g⁻¹ less than the soil-based system. The Chl. b content in the soil-based system is 1.21 mg g⁻¹, whereas in a hydroponic system, it is 1.321 mg g⁻¹, which is 0.111 mg g⁻¹ higher than the soil-base system.

IV. CONCLUSION

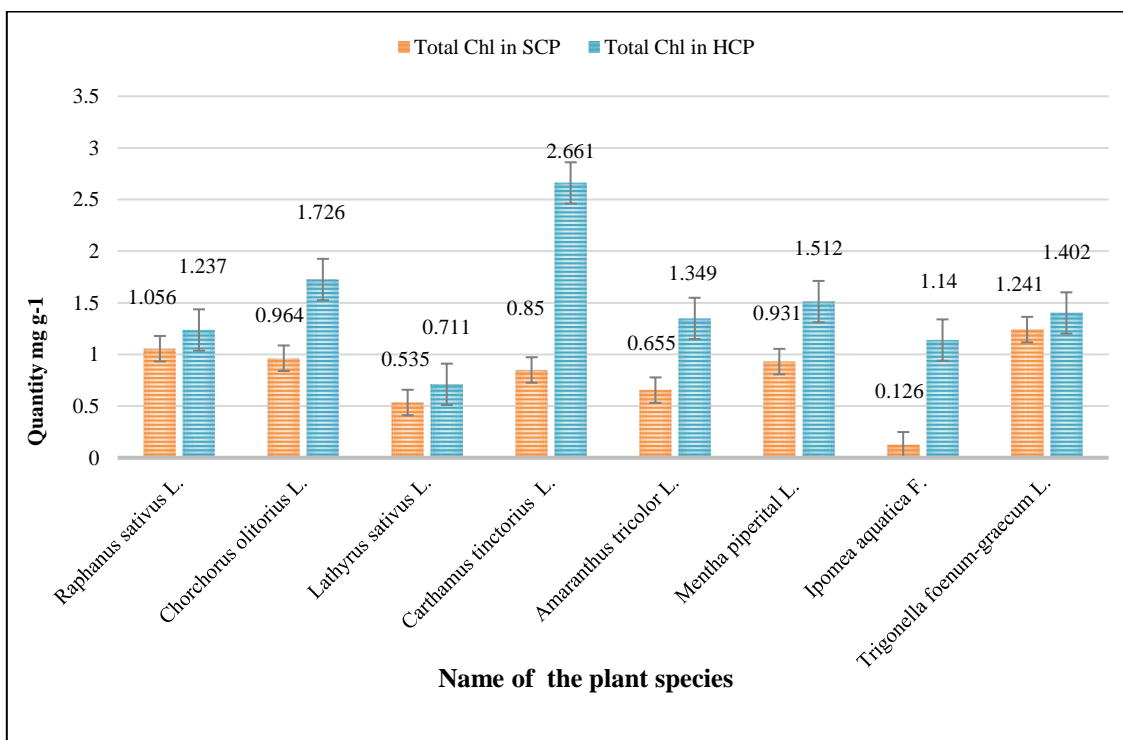
The study provides reliable data on chlorophyll content for a comparative analysis of soil and hydroponically cultivated plants in eight different species of leafy vegetables. The quantitative analysis of photosynthetic pigments showed that hydroponically grown plants of all eight species exhibit a stable and high total chlorophyll content compared to soil-based plants. In terms of chl_b, hydroponically cultivated plants show higher chl_b values than those grown in soil. However, the amount of chl_a is higher in soil-based plants for certain species such as *Raphanus sativus L.*, *Lathyrus sativus L.*, *Mentha piperita L.*, and *Ipomea aquatica F.* This difference occurs due to beneficial adaptations made by the plants. Furthermore, the chlorophyll content can be used as an indicator of plant health stress and nutritional deficiencies. These findings may be helpful for further comparative studies in soil and hydroponic cultivation.



Graph 1. The variation of chlorophyll a content in soil-cultivated plants and hydroponic-cultivated plants



Graph 2. The variation of chlorophyll b content in soil-cultivated plants and hydroponic-cultivated plants



Graph 3. The variation of Total chlorophyll content in soil-cultivated and hydroponic-cultivated plants

ACKNOWLEDGEMENT

I would want to express my sincere appreciation to Professor Amia Ekka, SoS in Life Science, Pt. RSU, Raipur. I also want to express my gratitude to all of the other support staff members specially Shri. Suresh sonkar,

Shri. Arun Jangade and Shri. Bhaiya Lal Sonkar they helped me out by providing the necessary equipment, without which I could not have completed this assignment as effectively.

REFERENCES

- [1] Arnon, D I, 1949. Copper enzymes in isolated chloroplasts. Polyphenoloxidase in Beta vulgaris. *Plant physiology* **24**(1): 1.
- [2] Chaturvedi, V D, Kumari V, Dubey N, Singh K, Singh P K, Chaubey S, Singh S, Singh P and Singh A, 2024. Analysis of chlorophyll. *Vegetable science* **51**(1): 154-163.
- [3] Devlin R M and Witham F H, 1997. Plant physiology, 4th edition. CBS Publications & Distributions, Delhi, pp. 223-242.
- [4] Dickmann D I and Kozlowski T T, 1968. Mobilization by Pinus resinosa cones and shoots of C-14 photosynthate from needles of different ages. *American Journal of Botany* **55**: 900-906.
- [5] Gogoi M and Basumatary M, 2018. Estimation of the chlorophyll concentration in seven Citrus species of Kokrajhar district, BTAD, Assam, India. *Tropical Plant Research* **5**(1): 83-87.
- [6] Kamble P N, Giri S P, Mane R S and Tiwana A, 2015. Estimation of Chlorophyll content in young and adult leaves of some selected plants. *Universal journal of environmental research and technology*, **5**(6): 306-310.
- [7] Kozlowski T T, Kramer J P and Pallardy G S, 1991. The physiological ecology of woody plants. Academic Press, Inc. San Diego. New York, pp. 37-44.
- [8] Pereyra M S, Davidenco V, Nunez S B and Argüello J A, 2014. Chlorophyll content estimation in oregano leaves using a portable chlorophyll meter: relationship with mesophyll thickness and leaf age. *Rev. Agronomía & Ambiente* **34**(1): 77-84.
- [9] Porra J R, 2002. The chequered history of the development and use of simultaneous equations for the accurate determination of chlorophyll a and b. *Photosynthesis research*, **73**: 149-156.
- [10] Prabhas L and Ekka A. Total chlorophyll determination in leafy vegetables cultivated in Hydroponics and Soil. **11**(2), 1584-1592.
- [11] Sadasivam S and Manickam A, 1996. Biochemical Methods," New Age International (P) Limited, New Delhi **2**: 124-126.
- [12] Xue L and Yang L, 2009. Deriving leaf chlorophyll content of green-leafy vegetables from hyperspectral reflectance. *ISPRS Journal of Photogrammetry and Remote Sensing* **64**(1): 97-106.

The Relationship Between Wave Period, Deep Water Wave and Breaking Wave Heights, Formulated Using the Wave Amplitude Function

Syawaluddin Hutahaean

Ocean Engineering Program, Faculty of Civil and Environmental Engineering-Bandung Institute of Technology (ITB), Bandung 40132, Indonesia

syawalf1@yahoo.co.id

Received: 30 Jul 2024,

Receive in revised form: 31 Aug 2024,

Accepted: 06 Sep 2024,

Available online: 12 Sep 2024

©2024 The Author(s). Published by AI Publication. This is an open-access article under the CC BY license

(<https://creativecommons.org/licenses/by/4.0/>).

Keywords— *Wave amplitude function, deep water and breaking wave height.*

Abstract— *The wave amplitude function is a relational equation that links wave amplitude with various water wave parameters, such as wave number, wave angular frequency, and wave constant. This function is derived by integrating the Kinematic Free Surface Boundary Condition over time. The wave amplitude function incorporates breaking characteristics, allowing for the extraction of breaking parameters, including breaking wave height, breaking wave length, and breaking water depth, as functions of the wave period. By combining the Euler momentum conservation equation with the wave amplitude function, a dispersion equation is obtained. This dispersion equation elucidates the relationships between deep water wave height, deep water wave length, and deep water depth in relation to the wave period. The results obtained for both deep water wave height and breaking wave height are consistent with previous research.*

I. INTRODUCTION

Water waves are commonly characterized by two key parameters: wave period and wave height. In the context of short waves, these parameters exhibit a one-to-one correspondence, meaning that a specific wave period is directly associated with a corresponding wave height. This correlation extends not only to deep water wave heights but also to breaking wave heights.

In this research, the correlation between deep water wave height and wave period, as well as between breaking wave height and wave period, has been systematically analyzed. The results are presented in the form of equations, tables, and graphical representations.

The relationship identified between deep water wave height and wave period aligns with the findings of Wiegel (1949, 1964), while the relationship between breaking wave height

and wave period is consistent with the research of Komar and Gaughan (1972).

These relationships are valuable for both practical engineering applications and research purposes. Practically, they enable quick estimation of deep water wave height and breaking wave height based solely on the wave period. In the research domain, the ongoing development of water wave transformation models, including processes like shoaling and breaking, necessitates reliable guidelines or estimates regarding the relationship between breaking wave height and wave period.

II. WEIGHTED TAYLOR SERIES AND WEIGHTING COEFFICIENT

In this article, a specialized equation and parameters are introduced that may not be widely recognized, namely the weighted Taylor series and the associated weighting coefficients.

The weighted Taylor series is a modified form of the traditional Taylor series, truncated to a first-order approximation. In this formulation, the contributions of higher-order terms are accounted for by incorporating weighting coefficients into the first-order differential term. Weighted Taylor series for function $f(x, t)$,

$$f(x + \delta x, t + \delta t) = f(x, t) + \gamma_{t,2} \delta t \frac{\partial f}{\partial t} + \gamma_x \delta x \frac{\partial f}{\partial x}$$

Weighted Taylor series for function $f(x, z, t)$,

$$f(x + \delta x, z + \delta z, t + \delta t) = f(x, z, t) + \gamma_{t,3} \delta t \frac{\partial f}{\partial t} + \gamma_x \delta x \frac{\partial f}{\partial x} + \gamma_z \delta z \frac{\partial f}{\partial z}$$

The weighting coefficients $\gamma_{t,2}$, $\gamma_{t,3}$, γ_x and γ_z are assigned base values of $\gamma_{t,2} = 2.0$, $\gamma_{t,3} = 3.0$, $\gamma_x = 1.0$ and $\gamma_z = 1.0$. There is no distinction between γ_x in the function $f(x, t)$ and γ_x in the function $f(x, z, t)$. The adjusted values of the weighting coefficients are functions of ϵ , the optimization coefficient, as detailed in Table 1. The method for calculating these weighting coefficients is described in Hutahaean (2023). For the purposes of this research, ϵ is set to 0.01.

Table 1. Corrected weighting coefficients values.

ϵ	$\gamma_{t,2}$	$\gamma_{t,3}$	γ_x	γ_z
0.010	1.9998	3.00465	0.99879	1.01093
0.011	1.99975	3.00563	0.99854	1.01325
0.012	1.99971	3.00671	0.99826	1.0158
0.013	1.99966	3.00788	0.99795	1.01858
0.014	1.99960	3.00915	0.99763	1.02159
0.015	1.99954	3.01052	0.99727	1.02484
0.016	1.99948	3.01198	0.9969	1.02832
0.017	1.99941	3.01355	0.99649	1.03205
0.018	1.99934	3.01521	0.99607	1.03601
0.019	1.99926	3.01697	0.99561	1.04022
0.020	1.99918	3.01883	0.99514	1.04468

In this work, a Cartesian coordinate system is employed, with x representing the horizontal axis and z denoting the vertical axis.

III. RESEARCH ON WAVE AMPLITUDE FUNCTION INTEGRATION RESULTS OF ORDER 0

Hutahaean (2024) integrated the Kinematic Free Surface Boundary Condition with respect to time using three levels of accuracy: 0th order, 2nd order, and 3rd order accuracy. The 0th order accuracy implies that the differential of the

water surface elevation is absent in the integration results, represented as $\frac{\partial^0 \eta}{\partial t^0}$, $\eta(x, t)$ is the water surface elevation function. The 2nd order accuracy includes the term $\frac{\partial^2 \eta}{\partial t^2}$, and the 3rd order accuracy incorporates the term $\frac{\partial^3 \eta}{\partial t^3}$.

The outcome of this integration is referred to as the wave amplitude function, which relates several wave parameters: wave amplitude A , wave number k , wave period T (expressed through the wave angular frequency $\sigma = \frac{2\pi}{T}$ and the wave constant G .

In the initial phase of this research, the focus is on the wave amplitude function derived from the 0th order accuracy integration. This research examines various aspects of wave parameters, including deep water wave height H_0 , deep water wavelength, critical deep water wave steepness, breaking wave height, breaking wavelength, and breaking water depth. The wave amplitude function resulting from the 0th order accuracy integration is as follows:

$$A = \frac{2Gk}{\gamma_{t,2}\sigma} \cosh \theta\pi \left(\frac{\tanh \theta\pi}{\sqrt{\gamma_z}} - \frac{kA}{2} \right) \dots\dots\dots(1)$$

A : wave amplitude

G : wave constant

σ : angular frequency, $\sigma = \frac{2\pi}{T}$, T is wave period.

k : is wave number

$\gamma_{t,2}$ and γ_z : are weighting coefficients

θ : deep water coefficient, where $\tanh \theta\pi \approx 1$.

The dispersion equation in deep water is derived from Euler's momentum conservation equation, under the assumption of negligible convective acceleration, and utilizing the wave amplitude function (Hutahaean, 2024). The resulting dispersion equation is as follows:

$$\frac{gA}{2} k^2 - \frac{g \tanh \theta\pi}{\sqrt{\gamma_z}} k + \gamma_{t,2}\gamma_{t,3}\sigma^2 = 0 \dots\dots\dots(2)$$

g gravitational acceleration and k wave number.

3.1. The relationship between wave period and deep water wave height

The relationship between wave period and deep water wave height, deep water wavelength and critical deep water wave steepness is formulated using (2).

The determinant value of (2) is,

$$d = \frac{g^2 \tanh^2 \theta\pi}{\gamma_z} - 2 gA\gamma_{t,2}\gamma_{t,3}\sigma^2$$

Given that the variable in the determinant equation is the wave amplitude A , and the wave period remains constant, there exists a maximum value of wave amplitude at which the determinant equals zero.

$$\frac{g^2 \tanh^2 \theta \pi}{\gamma_z} - 2 g A \gamma_{t,2} \gamma_{t,3} \sigma^2 = 0$$

Obtaining A_{max} ,

$$A_{max} = \frac{g \tanh^2 \theta \pi}{\gamma_z \gamma_{t,2} \gamma_{t,3} \sigma^2}$$

Or for $H = 2 A$,

$$H_{max} = \frac{2 g \tanh^2 \theta \pi}{\gamma_z \gamma_{t,2} \gamma_{t,3} \sigma^2}$$

This equation represents the relationship between wave height and wave period. For each wave period, there corresponds a unique wave height. Thus, it can be stated that for a given wave period, there is a specific wave height of:

$$H_0 = \frac{2 g \tanh^2 \theta \pi}{\gamma_z \gamma_{t,2} \gamma_{t,3} \sigma^2} \dots\dots\dots(3)$$

The index 0 on H indicates that the wave height refers to a condition unaffected by the sea bottom, representing the wave height in deep water.

When the determinant value is zero, the wave number in deep water, which is the root of equation (2), is given by:

$$k_0 = \frac{2 \tanh \theta \pi}{H_0 \sqrt{\gamma_z}} \dots\dots\dots(4)$$

$$L_0 = \frac{\pi H_0 \sqrt{\gamma_z}}{\tanh \theta \pi} \dots\dots\dots(5)$$

Substituting H_0 from equations (4) and (5) with the value obtained from equation (3) yields a direct relationship between deep water wavelength and wave period.

The deep water depth h_0 can then be calculated using the wave number conservation equation as detailed in Hutahaean (2023):

$$k \left(h + \frac{A}{2} \right) = \theta \pi \dots\dots\dots(6)$$

Where h is water depth. Therefore, deep water depth h_0 is,

$$h_0 = \frac{\theta \pi}{k_0} - \frac{H_0}{4}$$

The term "deep water" refers to the minimum water depth at which waves remain unaffected by the seabed. Both k_0 and H_0 are functions of the wave period, indicating that h_0 is likewise dependent on the wave period.

The calculated values of deep water wave height H_0 deep water wavelength L_0 , and minimum deep water depth h_0 are presented in Table 2. The calculations were conducted using $\theta = 1.928$ and $\varepsilon = 0.01$. It is noted that the impact of the deep water coefficient θ on the deep water wave height is minimal and can therefore be disregarded. The selection of $\theta = 1.94$ is associated with the breaking water depth, which will be explored in a subsequent section.

Since H_0 represents the maximum wave height, the wave steepness defined as $\frac{H_0}{L_0}$ can be referred to as the critical wave steepness. The calculation results indicate that $\frac{H_0}{L_0}$ is consistent across all wave periods, yielding a value of $\frac{H_0}{L_0} = 0.315$. In comparison, the critical wave steepness reported by Toffoli et al. (2010), which is $\frac{H_0}{L_0} = 0.170$ suggests that the critical wave steepness derived in this research is relatively high, although Toffoli et al. indicate that it can reach up to 0.20.

Table 2. Deep water wave parameter.

T (sec)	H ₀ (m)	L ₀ (m)	h ₀ (m)	H ₀ / L ₀
4	0.646	2.052	1.839	0.315
5	1.009	3.206	2.874	0.315
6	1.453	4.617	4.138	0.315
7	1.978	6.284	5.633	0.315
8	2.583	8.208	7.357	0.315
9	3.269	10.388	9.311	0.315
10	4.036	12.825	11.495	0.315
11	4.884	15.518	13.909	0.315
12	5.812	18.468	16.553	0.315
13	6.821	21.674	19.427	0.315
14	7.911	25.137	22.531	0.315
15	9.082	28.856	25.865	0.315
16	10.333	32.832	29.428	0.315
17	11.665	37.064	33.222	0.315
18	13.078	41.553	37.245	0.315

Wiegel (1949, 1964) formulated an equation to describe the relationship between deep water wave height and wave period as follows:,

$$H_{0-wieg} = \frac{gT^2}{15.6^2} \text{ m.} \dots\dots\dots(7)$$

The comparison with the Wiegel's equation is presented in Table 3 and illustrated in Figure 1, where the calculations were performed using the parameters $\theta = 1.928$ and $\varepsilon = 0.01$.

As shown in both Table 3 and Figure 1, the difference between the results is minimal, with a variance of only 0.131%. In Figure 1, the graphs representing H_0 and H_{0-wieg} overlap.

Table 3. Comparison to Wiegel's Equation (1949,1964)

T (sec)	H ₀ (m)	H _{0-wieg} (m)	$\frac{H_0 - H_{0-wieg}}{H_{0-wieg}} \times 100\%$
4	0.646	0.645	0.131
5	1.009	1.008	0.131
6	1.453	1.451	0.131
7	1.978	1.975	0.131
8	2.583	2.58	0.131
9	3.269	3.265	0.131
10	4.036	4.031	0.131
11	4.884	4.878	0.131
12	5.812	5.805	0.131
13	6.821	6.812	0.131
14	7.911	7.901	0.131
15	9.082	9.07	0.131
16	10.333	10.32	0.131
17	11.665	11.65	0.131
18	13.078	13.061	0.131

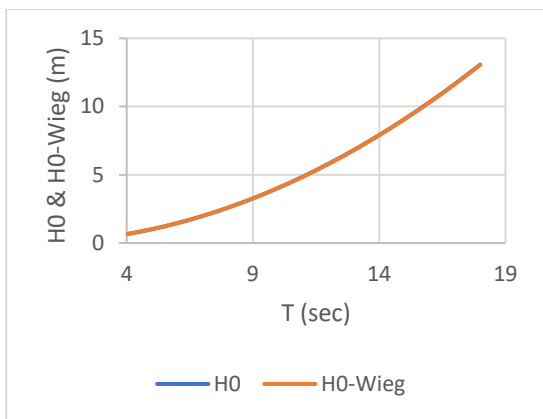


Fig.1: Comparison between H₀ to H_{0-wieg}

The purpose of this comparison is to demonstrate that previous research findings exhibit similar characteristics to those observed in this research. It is important to note that this research does not aim to derive an equation that replicates the wave height-wave period relationship described by the Wiegel's equation.

3.1. Relationship between wave period and breaking wave height

The relationship between breaking wave height and deep water wave height can be described using the principle of energy relationship. The wave energy equation, as formulated by Dean (1991), for one wavelength is given by:

$$E = c_E \rho g H^2 L$$

c_E energy coefficient, based on linear wave theory (Dean (1991)), $c_E = \frac{1}{8} \cdot \rho$ water mass density.

The results of the shoaling-breaking research using a numerical model with the wave amplitude function of order 0 indicate a loss of wave energy as the wave travels from deep water to the breaking point. Therefore, the relationship between the wave energy at the breaking point and the wave energy in deep water is expressed as follows:

$$E_b = 0.776 E_0$$

$$H_b^2 L_b = 0.776 H_0^2 L_0$$

Substitute (5)

$$H_b^2 L_b = 0.776 H_0^3 \frac{\pi \sqrt{\gamma_z}}{\tanh \theta \pi} \dots(8)$$

To determine L_b , the wave amplitude function equation (1) is used, which includes the breaking characteristic given by:

$$\frac{\tanh \theta \pi}{\sqrt{\gamma_z}} - \frac{kA}{2} = 0$$

Using the index b for breaking, thus,

$$\frac{k_b A_b}{2} = \frac{\tanh \theta \pi}{\pi \sqrt{\gamma_z}}$$

Given that $k_b = \frac{2\pi}{L_b}$ dan $H = 2A$, the relation is:

$$\frac{H_b}{L_b} = \frac{2 \tanh \theta \pi}{\pi \sqrt{\gamma_z}} \dots(9)$$

Or,

$$L_b = \frac{H_b \pi \sqrt{\gamma_z}}{2 \tanh \theta \pi}$$

Substituting into (8)

$$H_b^2 \frac{H_b \pi \sqrt{\gamma_z}}{2 \tanh \theta \pi} = 0.776 H_0^3 \frac{\pi \sqrt{\gamma_z}}{\tanh \theta \pi}$$

$$H_b = H_0 \cdot 1.552^{\frac{1}{3}}$$

Substituting H_0 from (3)

$$H_b = \frac{2 g \tanh^2 \theta \pi \cdot 1.552^{\frac{1}{3}}}{\gamma_z \gamma_{t,2} \gamma_{t,3} \sigma^2}$$

The final equation establishes a direct relationship between the breaking wave height and the wave period.

To determine the breaking water depth, the wave number conservation equation (6) is employed at the breaking point. This calculation utilizes the breaking wave height as a key parameter.

$$h_b = \frac{\theta \pi}{k_b} - \frac{H_b}{4}$$

In the subsequent section, the results of the calculations for the breaking parameters are presented, utilizing the calculation parameters $\varepsilon = 0.01$ and $\theta = 1.928$. The selection of $\theta = 1.928$ is intended to achieve a value of $\frac{H_b}{h_b} = 0.78$, which is a widely accepted criterion established by McCowan (1894). Decreasing the value of θ increases $\frac{H_b}{h_b}$ whereas increasing θ reduces $\frac{H_b}{h_b}$. However, the effect of θ on both H_0 and H_b is minimal, and it can be considered negligible. The value of $\frac{H_b}{L_b}$ can be calculated using equation (9), yielding a constant value of 0.633.

Table 4. Breaking parameter calculation results.

T (sec.)	H ₀ (m)	H _b (m)	L _b (m)	h _b (m)	$\frac{H_b}{h_b}$
4	0.646	0.748	1.188	0.958	0.78
5	1.009	1.168	1.856	1.497	0.78
6	1.453	1.682	2.673	2.156	0.78
7	1.978	2.29	3.638	2.935	0.78
8	2.583	2.991	4.752	3.833	0.78
9	3.269	3.785	6.014	4.851	0.78
10	4.036	4.673	7.424	5.989	0.78
11	4.884	5.655	8.983	7.246	0.78
12	5.812	6.729	10.691	8.624	0.78
13	6.821	7.898	12.547	10.121	0.78
14	7.911	9.16	14.552	11.738	0.78
15	9.082	10.515	16.705	13.475	0.78
16	10.333	11.963	19.006	15.331	0.78
17	11.665	13.506	21.456	17.308	0.78
18	13.078	15.141	24.055	19.404	0.78

Subsequently, a comparative analysis was performed using the breaking wave height equation proposed by Komar and Gaughan (1972), which is given by:

$$H_{b-KG} = 0.39 g^{1/5} (T_0 H_0^2)^{2/5} \dots(10)$$

The results of this comparison are detailed in Table (5) and illustrated in Figure (2). The analysis reveals a consistent relative difference of 1.047%.

Table 5. Comparison with the Breaking Wave Height Equation from Komar and Gaughan

T (sec)	H ₀ (m)	H _b (m)	H _{b-KG} (m)	δ (%)
4	0.646	0.748	0.756	1.047
5	1.009	1.168	1.181	1.047
6	1.453	1.682	1.7	1.047
7	1.978	2.29	2.314	1.047
8	2.583	2.991	3.023	1.047
9	3.269	3.785	3.825	1.047
10	4.036	4.673	4.723	1.047
11	4.884	5.655	5.714	1.047
12	5.812	6.729	6.801	1.047
13	6.821	7.898	7.981	1.047
14	7.911	9.16	9.256	1.047
15	9.082	10.515	10.626	1.047
16	10.333	11.963	12.09	1.047
17	11.665	13.506	13.649	1.047
18	13.078	15.141	15.301	1.047

Note : $\delta = \frac{H_b - H_{b-KG}}{H_{b-KG}} \times 100 \%$

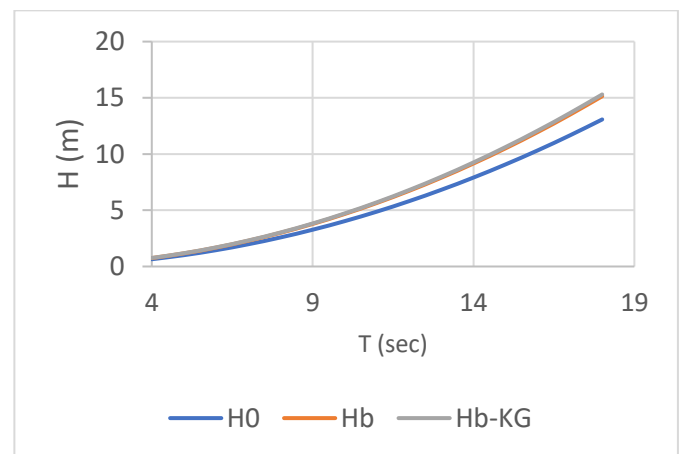


Fig.2: The comparison of breaking wave heights.

This research employs a zero-order wave amplitude function to derive simplified relationships between the wave period and various parameters: deep water wave height H_0 , deep water wavelength L_0 , deep water depth h_0 , and the wave steepness criterion $\frac{H_0}{L_0}$. It also establishes relationships with breaking wave height H_b , breaking wavelength L_b , breaking water depth H_b , and breaking wave steepness $\frac{H_b}{L_b}$.

Comparisons with deep water wave height estimates from Wiegel and breaking wave height calculations from Komar and Gaughan reveal that the results of this research are consistent with, or closely approximate, those of previous research.

IV. RESEARCH ON WAVE AMPLITUDE FUNCTION RESULT OF 3RD ORDER INTEGRATION

The wave amplitude function, derived from integrating the Kinematic Free Surface Boundary Condition with third-order accuracy (Hutahaean, 2024), is given by:

$$A = \frac{2Gk \cosh \theta \pi}{\sigma \gamma_{t,2}} \alpha_{kA} \dots(11)$$

$$\alpha_{kA} = \frac{\tanh \theta \pi}{\sqrt{\gamma_z}} + \left(\frac{3}{2\gamma_z} - \frac{3}{2} \right) kA - \frac{k^2 A^2}{2\sqrt{\gamma_x} \sqrt{\gamma_z}} \tanh \theta \pi + \left(\frac{1}{\gamma_z^2} - \frac{1}{\gamma_z} \right) \frac{k^3 A^3}{8}$$

The dispersion equation of third order is expressed as

$$\left(\frac{1}{\gamma_z^2} - \frac{1}{\gamma_z} \right) \frac{A^3}{8} k^4 - \frac{\tanh \theta \pi A^2}{2\sqrt{\gamma_x} \sqrt{\gamma_z}} k^3 + \left(\frac{1}{2\gamma_z} - \frac{3}{2} \right) A k^2 + \frac{\tanh \theta \pi}{\sqrt{\gamma_z}} k - \frac{\gamma_{t,3} \gamma_{t,3} \sigma^2}{g} = 0 \dots \dots(12)$$

4.1. The calculation of deep water wave height H_0 .

Equation (12) exhibits a characteristic where there is a maximum wave amplitude value, A_{max} beyond which any further increase in amplitude results in a wave number value that becomes zero or negative. This suggests that Equation (12) has a discontinuity at A_{max} .

To determine A_{max} , calculations are performed iteratively, starting from a small wave amplitude value and incrementally increasing it by a small amount. In this research, an increment of 0.0001 is used until A_{max} is obtained.

Given that the equation is a fourth-degree polynomial, the Newton-Raphson method is employed for the iterative calculation. To initiate the iteration, the equation is simplified by assuming that k^3 and k^4 are negligibly small, reducing the problem to a second-degree polynomial, which is expressed as follows:

$$\left(\frac{1}{2\gamma_z} - \frac{3}{2} \right) A k^2 + \frac{\tanh \theta \pi}{\sqrt{\gamma_z}} k - \frac{\gamma_{t,3} \gamma_{t,3} \sigma^2}{g} = 0$$

In this equation, there are two values of k for each wave amplitude A and positive value is selected. Consequently, the calculation process involves two stages for each wave

amplitude value. Initially, the wave number k is approximated using a simplified equation, which provides an estimated value of k . Following this approximation, the Newton-Raphson method is employed to refine the value of k by applying it to the complete dispersion equation. This two-stage approach enhances the accuracy of the calculated wave number k for the given wave amplitude A .

The calculation results using $\theta = 1.3395$, $\varepsilon = 0.01$ are presented in Table (6).

Table 6. Results of Wave Parameter Calculations in Deep Water.

T (sec)	H_0 (m)	L_0 (m)	h_0 (m)	$\frac{H_0}{L_0}$
4	0.68	2.735	1.661	0.249
5	1.063	4.262	2.588	0.249
6	1.53	6.129	3.721	0.25
7	2.083	8.291	5.03	0.251
8	2.721	10.85	6.584	0.251
9	3.443	13.746	8.342	0.25
10	4.251	16.935	10.275	0.251
11	5.144	20.46	12.412	0.251
12	6.122	24.326	14.756	0.252
13	7.184	28.538	17.31	0.252
14	8.332	33.088	20.069	0.252
15	9.565	37.941	23.01	0.252
16	10.883	43.246	26.232	0.252
17	12.287	48.746	29.564	0.252
18	13.775	54.682	33.166	0.252

The values of H_0 and L_0 calculated using the third-order dispersion equation are larger than those obtained from the zeroth-order dispersion equation. Additionally, the critical wave steepness $\frac{H_0}{L_0}$ is smaller for the third-order results, averaging 0.250, compared to the zeroth-order result of $\frac{H_0}{L_0} = 0.315$. Thus, the critical wave steepness derived from the third-order calculation is closer to the criteria proposed by Toffoli et al. (2010), which range from $\frac{H_0}{L_0} = 0.17-0.2$.

However, it is important to note that this research does not aim to match the critical wave steepness criteria set by Toffoli et al.

Table 7. The Comparison between H_0 and H_{0-wieg} .

T (sec)	H_0 (m)	H_{0-wieg} (m)	$\frac{H_0 - H_{0-wieg}}{H_{0-wieg}} \times 100\%$
4	0.68	0.645	5.431
5	1.063	1.008	5.441
6	1.53	1.451	5.445
7	2.083	1.975	5.457
8	2.721	2.58	5.454
9	3.443	3.265	5.453
10	4.251	4.031	5.456
11	5.144	4.878	5.458
12	6.122	5.805	5.459
13	7.184	6.812	5.459
14	8.332	7.901	5.462
15	9.565	9.07	5.463
16	10.883	10.32	5.464
17	12.287	11.65	5.466
18	13.775	13.061	5.469

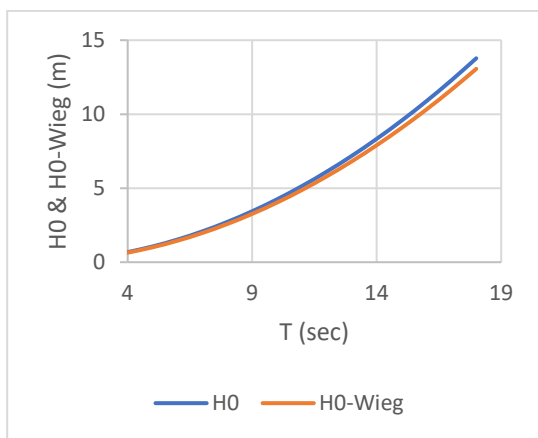


Fig.3: The Comparison between H_0 and H_{0-wieg}

Next, the wave height H_0 is compared with the deep water wave height H_{0-wieg} from Wiegel, as presented in Table 7 and Figure 3. The average difference between H_0 and H_{0-wieg} is 5.45%, whereas the difference using the zeroth-order dispersion equation is only 0.131%. It is important to note that this research does not aim to replicate Wiegel's (1949, 1964) deep water wave height results precisely. The comparison serves to demonstrate that the findings are in general agreement with existing research.

4.2. Calculation of breaking parameters H_b , L_b and h_b

The calculation of breaking parameters is performed using the breaking characteristics outlined in Equation (11):

$$\frac{\tanh \theta \pi}{\sqrt{\gamma_z}} + \left(\frac{3}{2\gamma_z} - \frac{3}{2} \right) kA - \frac{k^2 A^2}{2\sqrt{\gamma_x \sqrt{\gamma_z}} \tanh \theta \pi} + \left(\frac{1}{\gamma_z^2} - \frac{1}{\gamma_z} \right) \frac{k^3 A^3}{8} = 0 \quad \dots\dots\dots(13)$$

This equation is a third-degree polynomial, which precludes the formulation of a simple equation for breaking wave steepness. However, the equation allows for the calculation of the kA value under breaking conditions. For example:

$$k_b A_b = \alpha$$

Therefore,

$$\frac{H_b}{L_b} = \frac{\alpha}{\pi}$$

Or,

$$L_b = \frac{\pi H_b}{\alpha} \quad \dots\dots(14)$$

The calculation process is carried out in stages. In the first stage, a second-degree polynomial approximation is applied by neglecting the term containing $k^3 A^3$ in equation (13), under the assumption that this term is negligible.

$$\frac{\tanh \theta \pi}{\sqrt{\gamma_z}} + \left(\frac{3}{2\gamma_z} - \frac{3}{2} \right) kA - \frac{k^2 A^2}{2\sqrt{\gamma_x \sqrt{\gamma_z}} \tanh \theta \pi} = 0$$

This equation has two roots, with the smallest kA value being selected. Using this initial result, further calculations are performed with equation (13) using the Newton-Raphson iteration method.

The results of the shoaling-breaking research using a numerical model with the wave amplitude function of order 3 indicate a loss of wave energy as the wave travels from deep water to the breaking point. Therefore, the relationship between the wave energy at the breaking point and the wave energy in deep water is expressed as follows:

$$E_b = 0.8 E_0$$

Once the α value is determined, the breaking wave height H_b is calculated using the energy conservation equation:

$$H_b^2 L_b = 0.8 H_0^2 L_0$$

Substituting L_b ,

$$H_b^3 = \frac{0.8\alpha}{\pi} H_0^2 L_0$$

With the obtained H_b value, L_b can be calculated using equation (14), and the breaking water depth is determined with the wave number conservation equation:

$$h_b = \frac{\theta \pi}{k_b} - \frac{H_b}{4}$$

Table (8) presents the results of the breaking parameter calculations. These calculations were performed with $\epsilon = 0.01$ dan $\theta = 1.3395$. This value of θ yields $\frac{H_b}{h_b} = 0.781$, which differs from the zero-order calculation, which requires $\theta = 1.928$ to achieve $\frac{H_b}{h_b} = 0.78$. The calculated breaking wave steepness is $\frac{H_b}{L_b} = 0.438$, which is smaller than the zero-order breaking wave steepness of $\frac{H_b}{L_b} = 0.633$.

Table 8. Results of Calculation of Breaking Parameters with Wave Amplitude Function Accuracy of Order 3

T (sec)	H _b (m)	L _b (m)	h _b (m)	$\frac{H_b}{L_b}$	$\frac{H_b}{h_b}$
4	0.68	0.762	0.976	0.438	0.781
5	1.063	1.19	1.524	0.438	0.781
6	1.53	1.713	2.193	0.438	0.781
7	2.083	2.327	2.979	0.438	0.781
8	2.721	3.041	3.894	0.438	0.781
9	3.443	3.85	4.93	0.438	0.781
10	4.251	4.75	6.082	0.438	0.781
11	5.144	5.744	7.356	0.438	0.781
12	6.122	6.834	8.751	0.438	0.781
13	7.184	8.019	10.269	0.438	0.781
14	8.332	9.298	11.906	0.438	0.781
15	9.565	10.67	13.664	0.438	0.781
16	10.883	12.149	15.558	0.438	0.781
17	12.287	13.709	17.555	0.438	0.781
18	13.775	15.374	19.687	0.438	0.781

Next, the breaking wave height is compared with the breaking wave height from the Komar-Gaughan equation (10). The results of this comparison are detailed in Table (9) and illustrated in Figure (4). The average difference between the two measurements is 3.5%, with H_b consistently smaller than H_{b-KG}.

Table 9. Comparison between H_b and the breaking height Komar-Gaughan H_{b-KG}.

T (sec)	H ₀ (m)	H _b (m)	H _{b-KG} (m)	δ (%)
4	0.68	0.762	0.787	3.214
5	1.063	1.19	1.231	3.301
6	1.53	1.713	1.772	3.342

7	2.083	2.327	2.412	3.541
8	2.721	3.041	3.15	3.48
9	3.443	3.85	3.987	3.446
10	4.251	4.75	4.923	3.513
11	5.144	5.744	5.956	3.562
12	6.122	6.834	7.089	3.592
13	7.184	8.019	8.319	3.604
14	8.332	9.298	9.649	3.637
15	9.565	10.67	11.076	3.667
16	10.883	12.149	12.603	3.595
17	12.287	13.709	14.227	3.644
18	13.775	15.374	15.951	3.617

Note : $\delta = \frac{H_b - H_{b-KG}}{H_{b-KG}} \times 100\%$

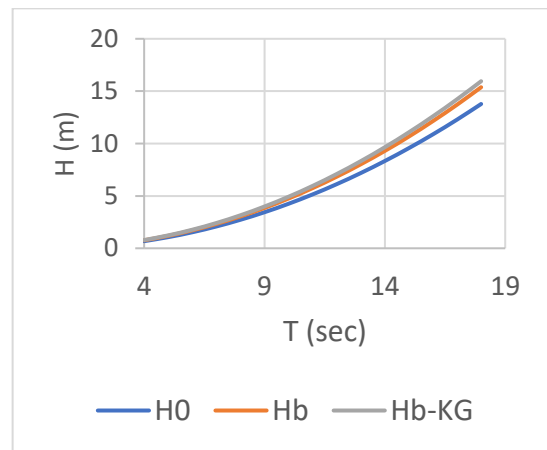


Fig.4: The comparison between H_b and H_{b-KG}

The research on breaking wave height, utilizing a third-order wave amplitude function, yielded results that differ from the breaking wave height values provided by Komar and Gaughan, with an average difference of 3.5%. Given this relatively small discrepancy, the relationship between breaking wave height and wave period can be effectively applied using either of the two methods.

V. CONCLUSIONS

The analysis concludes that the relationship between deep water wave height and wave period shows qualitative consistency across the three methods examined: the zero-order wave amplitude function, the third-order approximation, and the Wiegel's method. Despite this similarity in quality, the quantitative results suggest that one of these methods should be chosen for practical applications.

Between the zero-order and third-order approximations, the third-order method is preferred for its superior accuracy in representing critical deep water wave steepness, aligning more closely with other research findings.

For breaking wave height, the zero-order approximation, third-order method, and Komar-Gaughan approach are qualitatively equivalent. However, the selection of a method should be based on quantitative considerations.

In terms of breaking wave steepness, the third-order approximation provides more accurate results than the zero-order method.

For practical and engineering applications, the zero-order wave amplitude function is recommended due to its simplicity and ease of implementation.

The wave energy equation utilized in this study is based on a sinusoidal wave profile. However, given that the wave profile at larger wave heights tends to be cnoidal or solitary, it is essential to develop a wave energy equation tailored to these wave profiles.

REFERENCES

- [1] Wiegel, R.L. (1949). An Analysis of Data from Wave Recorders on the Pacific Coast of the United States, *Trans. Am. Geophys. Union*, Vol.30, pp.700-704.
- [2] Wiegel, R.L. (1964). *Oceanographical Engineering*, Prentice-Hall, Englewood Cliffs, N.J.
- [3] Komar, P.D. & Gaughan M.K. (1972). Airy Wave Theory and Breaker Height Prediction, *Coastal Engineering Proceedings*, 1 (13).
- [4] Hutahaean, S. (2023). Method for Determining Weighting Coefficients in Weighted Taylor Series Applied to Water Wave Modeling. *International Journal of Advance Engineering Research and Science (IJAERS)*. Vol. 10, Issue 12; Dec. 2023, pp 105-114. Article DOI: <https://dx.doi.org/10.22161/ijaers.1012.11>.
- [5] Hutahaean, S. (2024). Enhance of Integration of Kinematic Free Surface Boundary Condition to Third Order Accuracy for Wave Transformation Modeling. *International Journal of Advance Engineering Research and Science (IJAERS)*. Vol. 11, Issue 7; Jul, 2024, pp 55-67. Article DOI: <https://dx.doi.org/10.22161/ijaers.117.6>.
- [6] Toffoli, A., Babanin, A., Onaroto, M. and Wased, T. (2010). Maximum steepness of oceanic waves : Field and laboratory experiments. *Geophysical Research Letters*. First published 09 March 2010. <https://doi.org/10.1029/2009GL0441771>
- [7] Dean, R.G., Dalrymple, R.A. (1991). *Water wave mechanics for engineers and scientists*. Advance Series on Ocean Engineering.2. Singapore: World Scientific. ISBN 978-981-02-0420-4. OCLC 22907242.
- [8] Mc Cowan, J. (1894). On the highest waves of a permanent type, *Philosophical Magazine, Edinburgh* 38, 5th Series, pp. 351-358.

Research on heat transfer model prediction of Tesla Valve heat sink based on training neural network method

Yan-Xiao Jia, Yan-Zuo Chang*, Guo-Xing Yang, Ruo-Yu Yang, Yi-wei Zhang, Ting-Hao Zhang

Energy and Power Engineering, Guangdong University of Petrochem Technology (GDUPT), Maoming, 525000, China
(Corresponding author: Yan-Zuo Chang PhD), Email: qq3102492448@163.com

Received: 12 Aug 2024,

Receive in revised form: 12 Sep 2024,

Accepted: 19 Sep 2024,

Available online: 23 Sep 2024

©2024 The Author(s). Published by AI
Publication. This is an open-access article under
the CC BY license

(<https://creativecommons.org/licenses/by/4.0/>).

Keywords— *Tesla valve heat sink, neural network, CFD numerical simulation.*

Abstract— *With the increasing power density of electronic equipment, heat dissipation technology has become the key to ensure the stable operation of equipment. Because of its unique structural design, the Tesla valve heat sink shows great potential in the heat dissipation of high-power electronic devices. However, the traditional heat transfer model prediction method has the problems of complex calculation and low efficiency. The purpose of this study is to explore a method of heat transfer model prediction based on training neural network to improve the accuracy and efficiency of heat transfer efficiency prediction of Tesla valve heat sink. The heat transfer data of Tesla valve heat sink under different structures were collected by numerical simulation. The data were then used to train a feed forward neural network. Through a lot of training and verification, the neural network model shows good generalization ability and can accurately predict the heat transfer efficiency under unknown conditions. In this study, the effects of network structure, training algorithm and optimization strategy on model performance are discussed, and an improved network architecture is proposed to improve the accuracy of prediction. Finally, the advantages of the proposed method in computational efficiency and prediction accuracy are verified by comparison with traditional methods.*

I. INTRODUCTION

In the rapid development of electronic technology, the performance leap of high-power density electronic devices is closely related to the improvement of heat dissipation efficiency [1]. With the miniaturization and high frequency of integrated circuits and the continuous rise of computing speed, the heat generated inside electronic devices has increased sharply, and the heat dissipation problem has become one of the key factors restricting its performance bottleneck. With its unique geometric structure and excellent heat transfer performance, the Tesla valve heat

sink is considered as one of the new generation of efficient heat dissipation solutions [2].

The Tesla valve, through a carefully designed asymmetric flow channel structure, enables the fluid to flow efficiently in a specific direction, while being significantly hindered in the opposite direction. This feature not only improves the heat dissipation efficiency, but also reduces energy consumption, providing a strong guarantee for the efficient and stable operation of electronic equipment. Domestic and foreign scholars continue to deepen the research of Tesla valve, from the basic flow characteristics analysis to the complex heat

transfer performance optimization, each progress indicates its broad application prospects in the future heat dissipation technology.

At present, the research of Tesla valve has covered multiple dimensions. The study of Thompson et al. [3] revealed the effects of valve spacing, series and Reynolds number on the performance of multistage Tesla valves, providing a theoretical basis for design optimization [3]. S.F. de Vries et al. verified the feasibility of the new Tesla valve in enhancing heat transfer through innovative design, combined with steady-state two-phase flow experiment and laminar single-phase simulation, and further promoted the application of Tesla valve in high-efficiency heat dissipation systems such as heat pipes [4]. Based on the Fluent simulation platform, Ren Pu studied the fluid flow characteristics of the Tesla valve during reverse navigation, and also analyzed the causes of cavitation in the Tesla valve and the influence of the cavitation model on the fluid flow [9]. In recent years, artificial intelligence technology and neural network technology have provided new possibilities to solve this problem.

In the early 1990s, the personal computer (PC) era was represented by the Intel 80486 microprocessor (486 era), the CPU power consumption is relatively low, such as the maximum power consumption of Intel 486DX4 processor reached 5W, the heat dissipation demand is not high, the design of the radiator is usually more simple, generally using the passive heat dissipation of static heat sink, or equipped with a small fan to achieve active heat dissipation. With the increase of CPU frequency, such as the introduction of Intel Pentium series, power consumption and heat began to increase, and power consumption was also greatly increased to 11.2w, and the radiator began to be equipped with a fan, forming the prototype of an air-cooled radiator. In the Pentium III and IV era, the power consumption and heat output of the CPU increased sharply, and the volume of the radiator increased accordingly, and copper base, plug copper and copper-aluminum combined fin radiator appeared to improve the heat dissipation efficiency.

However, the complex structure of Tesla valve makes its flow and heat transfer mechanism difficult to be fully explained by traditional theories, especially under complex conditions such as high flow rate and multiphase flow, its performance prediction and optimization face many difficulties. In addition, existing prediction models often rely on large amounts of experimental data, which are expensive to compute and difficult to respond quickly to design changes.

To solve these problems, artificial intelligence technology and neural network technology are introduced

in this study. Because of its powerful nonlinear mapping ability and self-learning ability, neural network can construct accurate prediction model. The prediction method of heat transfer mode of Tesla valve heat sink based on training neural network is the concrete practice of this idea. We aim to explore a method for predicting heat transfer mode of Tesla valve heat sink based on training neural network, in order to improve the accuracy and computational efficiency of prediction [5][6][7][8].

In this paper, CFD numerical simulation technology is first used to build a variety of Tesla valve models, and simulation analysis is carried out under the same working conditions, and detailed heat transfer data including inlet and outlet pressure difference, Nussel number, and geometric structure parameters are collected. These data will serve as the "nourishment" for neural network training and provide a solid foundation for model construction.

A feedforward neural network is then designed and trained, which realizes complex mapping of the heat transfer performance of the Tesla valve through the connection and activation of multiple layers of neurons. In the training process, the network structure is optimized and the hyperparameters are adjusted to improve the prediction accuracy and generalization ability of the model. At the same time, the influence of two key parameters, the length of the flow channel section and the Angle of the valve, on the heat transfer performance is studied, and a new way to optimize the structure of the Tesla valve is explored by adjusting these parameters.

This study is expected to establish a set of neural network-based heat transfer performance prediction model of Tesla valve heat sink, which can accurately and efficiently predict heat transfer performance of different structures of Tesla valves, and provide strong support for the design and optimization of heat sink.

As an important cooling element in electronic products, the development history of electronic heat sink closely follows the evolution of electronic technology. With the improvement of the performance of electronic products, heat dissipation technology is also constantly improving and innovating [10].

The research significance of this paper comes from the use of CFD numerical simulation to collect heat transfer data of different Tesla valve models under the same working conditions, including inlet and outlet pressure difference, Nussel number, geometric structure parameters, etc. Then design and train a feedforward neural network, establish a training model, and adjust the grid structure. The influence of two parameters, the length of the flow channel section and the Angle of the valve, on the heat transfer performance of the Tesla valve was studied, and

the optimization algorithm was finally able to improve the generalization ability and prediction accuracy of the model. The prediction model was used to predict the heat transfer performance of different structures and optimize the structure of the Tesla valve [11][12].

II. TESLA VALVE MODEL ESTABLISHMENT AND CFD PRE-TREATMENT

Since Tesla valves are mostly used in electronic products, the size of the design in this paper will be determined according to the size of electronic products. CAD is used to establish a two-dimensional geometric model, and 3D is generated by the built-in modeling tool in ANSYS2022. Then Mesh in ANSYS2022 is used to divide the model and name the boundary.

2.1 Initial selection of the Tesla valve geometry model

The average length of the Tesla valve designed in this paper is 100mm. As shown in Figure 1, the width of the flow channel section is fixed at 3mm, the length is D , and the valve Angle is α . These two geometric parameters change within the specified range, while the remaining parameters remain unchanged. Each Tesla valve is a one-stage, and this paper designs a two-stage Tesla valve. The fluid in the channel is water, and its physical properties change with temperature. Wall material is copper.

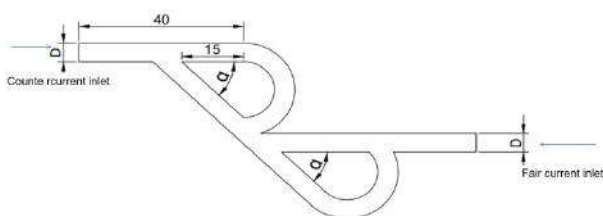


Fig. 1: Sample size of Tesla valve/mm

Tesla valve in the counter current process will appear some unique fluid mechanics phenomena, these phenomena are the result of its unique geometric structure and the physical characteristics of the fluid. Some key hydrodynamic phenomena such as increased flow rate, decreased pressure, cavitation effect, eddy current formation, fluid separation, enhanced heat exchange, flow asymmetry, turbulent transition, hydrodynamic instability, and energy dissipation may occur during the counter current process of the Tesla valve.

The speed of the upstream inlet and the upstream inlet is 0.05m/s, and the rest remain unchanged. The exit domain is set as the exit boundary. The fluid can effectively avoid the wing-like barrier and flow from the right to the left unimpeded, and the effect of acceleration is obtained due

to the flow pressure, and the speed has been accelerating in the main channel, the speed is close to 0.1m/s; When fluid flows in reverse, it encounters a wing-like barrier. Whenever fluid passes through one of these channels, it flows into a wing-like barrier due to inertia. The shock of back flow and the sudden increase in pressure can prevent the fluid from moving forward, making it difficult to pass through the valve. The more wing-shaped obstacles, the more resistance the fluid is subjected to in the reverse flow, which creates the one-way flow characteristics of the Tesla valve.

A monitoring point is provided at the reverse flow inlet through road, near the oblique channel, to monitor the speed and pressure at the point.

III. NEURAL NETWORK

Artificial neural network (ANN) or analog neural network (SNN). These networks consist of interconnected neurons, divided into input layers, one or more hidden layers, and output layers, where neurons perform mathematical operations on input data and pass the results to the next layer, allowing the network to learn complex patterns and relationships in the data. Each node in the neural network receives input processing and passes the output to the next node[13] [14] [15].

Import Fluent simulation data results into the MATLAB workspace. The four data of upstream N_{uf} , counter-current N_{ur} , relative performance evaluation standard RPEC and D_i are imported into the work area as labels, and the output form is a numerical matrix, denoted as "T". The length of the section of the flow channel and the Angle of the valve are imported into the work area as features, and the output form is a numerical matrix, denoted as "X"; Set several sets of parameters as shown in Table 1, and import them into the work area as prediction objects. The output form is a numerical matrix, which is denoted as "YC".

Table.1: Predicted parameters

Forecasting group	The length of the flow channel section/mm	Valve Angle/°
Forecasting 1	3	33
Forecasting 2	5	44
Forecasting 3	7	55
Forecasting 4	7	33
Forecasting 5	5	55
Forecasting 6	3	44

There are 9 samples in total. The 9 samples are divided into three parts: 70% training set, 15% verification set and 15% test set. In other words, 7 samples are taken as training set, 1 sample as verification set and 1 sample as test set. Using the least square method, it occupies a large memory, takes the least time, and can be automatically

stopped. The results include Neural Network part, Algorithms part, Progress part and Plot part.

Save the trained neural network model, use the training model to predict the previously designed prediction parameters, and get the result "Y". The results are summarized in Table 4.

IV. INTERPRETATION OF RESULT

4.1 Fluent Simulation result analysis

Table 2 Simulated result

Experimental group	Downstream pressure drop $\Delta P_f/Pa$	Counter-current pressure drop $\Delta P_r/Pa$	Downstream Nu _f	Counter-current Nur	Di	RPEC
Test1	20.56	22.37	197.06	203.06	1.088	1.002
Test2	21.69	23.19	172.45	178.54	1.069	1.013
Test3	24.46	25.47	140.26	143.3	1.041	1.008
Test4	14.59	15.76	208.09	216.62	1.08	1.015
Test5	16.11	17.5	185.05	194.68	1.086	1.024
Test6	18.33	19.6	152.37	159.93	1.069	1.026
Test7	12.87	14.09	227.92	247.3	1.095	1.008
Test8	14.34	15.76	215.13	226.38	1.099	1.02
Test9	16.42	17.57	179.63	188.93	1.07	1.028

Table 3 Forecast summary

Forecasting group	Fair current Nu _f	Adverse current Nur	Di	RPEC
Forecasting 1	196.5961	202.6147	1.0858	1.0038
Forecasting 2	188.0456	198.3291	1.0925	1.0245
Forecasting 3	183.1189	191.6469	1.0669	1.0249
Forecasting 4	235.6566	246.1588	1.0942	1.0098
Forecasting 5	164.1569	170.9464	1.0734	1.0235
Forecasting 6	176.9233	183.1591	1.0717	1.0075

Upflow Nu and counter flow Nur vary as the valve Angle increases. When the valve Angle is small, the Nu value is higher and the heat transfer effect is better. This may be because the smaller valve Angle helps the fluid form more vortex and turbulence inside the Tesla valve, which enhances heat transfer. However, as the valve Angle increases, the Nu value decreases, which may be due to the energy loss caused by the increase in the fluid flow path. The pressure drop data show that the down-flow pressure drop ΔP_f and the counter-flow pressure drop ΔP_r decrease as the valve Angle increases. This may be because the larger valve Angle helps the fluid flow through the valve more smoothly, reducing the resistance of the fluid. However, too low a valve Angle can result in too large a pressure drop, which can affect the overall performance of the Tesla valve. RPEC is used as a comparison of the overall performance of the Tesla valve in reverse flow and forward flow, and the closer the value is to 1, the better the performance. The RPEC value does not monotonically increase with increasing cross section length, which indicates that the design of the Tesla valve needs to find a balance between heat transfer efficiency and fluid flow resistance. The Di parameter is used as a measure of single flow, and its value reflects the resistance of the valve to counter current. As shown in Table 3, Di values are lower in some test groups, which may mean that these Tesla valve designs are more effective at preventing backflow.

The length of the cross section also affects the performance of the Tesla valve. Increasing the cross section length helps to increase the Nu value and thus the heat transfer performance, but it may also lead to an increase in pressure drop. This shows that when designing the Tesla valve, it is necessary to consider the heat transfer efficiency and the resistance of the fluid flow to achieve the optimal design. In summary, the valve Angle of the Tesla valve and the cross section length of the flow channel have a significant impact on its heat transfer performance. Smaller valve Angle is beneficial to increase Nu value, but may lead to increased pressure drop. The larger cross section length helps to improve the heat transfer performance, but may be unfavorable to the single conduction. Therefore, the design of the Tesla valve needs to consider multiple factors, by optimizing the valve Angle and cross section length to balance the heat transfer efficiency and fluid flow resistance to achieve the best heat dissipation results. In addition, the difference between the predicted results of the neural network model and the simulated data suggests that the model may require more training data or a more complex network structure to improve the prediction accuracy. Future research could further explore the optimal combination of these parameters and optimize the design of the Tesla valve through experimental validation.

The parts of Tesla valve where heat transfer is enhanced generally appear in the parts where turbulence is intensified, cavitation phenomenon is significant and eddy current is generated, and the speed of these parts will be significantly different from other parts. Now, the influence of valve Angle and flow channel section length on the heat transfer performance of Tesla valve is analyzed respectively.

Test1, test2, test3, the cross section length of the flow channel of the three experimental groups is 3mm, and their valve angles are 30°, 45°, and 60° respectively. According to the simulation results, Nu at 30° is the highest among the three groups, indicating the best heat transfer effect.

The fluid of the curve and the fluid of the straight passage have impact interaction at the junction, resulting in three low flow rate areas, the pressure drops sharply, the speed increases, resulting in cavitation phenomenon, and then enters the low flow rate area, the pressure increases, and the cavitation bubble disappears. As the valve Angle increases, the Angle of fluid interaction between the bend and the straight passage decreases, and the cavitation effect weakens. As can be seen from the figure, the cavitation region of test2 and test3 is smaller than that of test1, and the cavitation phenomenon can enhance the effect of heat transfer, so the Nu of test1 is the largest among the three.

The heat transfer performance of the Tesla valve is closely related to the flow state of the internal fluid. Under counter current conditions, the flow of fluid inside the valve is impeded, and this obstruction causes the fluid to separate in some parts of the valve, forming a flow separation zone. These separation zones can lead to local stagnation of the fluid, which affects heat transfer efficiency. However, this flow separation also increases the contact time between the fluid and the valve wall, helping to improve heat exchange efficiency. Especially when the flow separation zone is accompanied by the formation of eddy currents, this situation will cause the fluid to further enhance the heat exchange effect with the wall, because the eddy currents can promote the heat mixing and transfer inside the fluid. With the increase of cross section length, Nu value increases and heat transfer performance is enhanced. At the same time, turbulent flow occurs in a larger flow channel, and the probability of eddy current increases. These unstable flows are also responsible for enhanced heat transfer.

The larger the cross section length of the flow channel, the fluid will gradually become obstructed under the condition of forward flow. More and more fluid will enter the curved channel due to inertia, showing the effect of obstructing fluid flow similar to that under the counter current condition, indicating that the increase in the cross section length will increase the probability of fluid entering the curved channel at the intersection of the straight channel and the curved channel. This is not good for optimizing the single pilot connectivity of the Tesla valve.

Changes in the cross section length of the flow channel also affect the heat transfer performance and cavitation phenomenon of the Tesla valve. Increasing the cross section length can increase the heat transfer area and thus improve the heat transfer efficiency. However, excessive cross section lengths may lead to increased impediments to fluid flow, reducing the occurrence of turbulence and eddy currents, and thus reducing heat transfer efficiency. Therefore, the design of Tesla valves requires a balance between heat transfer efficiency and fluid flow resistance.

Equivalent points are set at the entrance, exit, middle interchange and bend of the Tesla valve of test1 and test5, respectively, to monitor the speed and pressure changes in the channel under the condition of forward flow and reverse flow. The specific location is shown in Table 1.

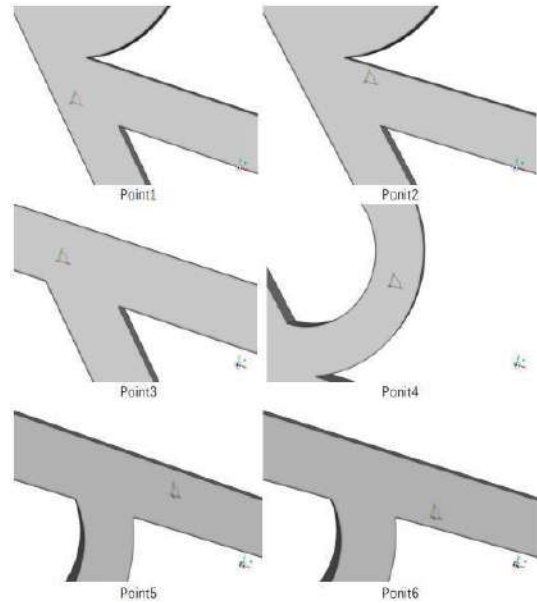


Fig. 2 Set equivalent points

The equivalent points Point1 and Point2 at the middle interchange are used to monitor the velocity difference when the fluid cavitation occurs here in the case of counter current. Subjectively, it is believed that these two points will produce a large velocity difference in the case of counter current, while in the case of forward flow, it will not produce a large velocity difference. The equivalent point Point3 at the entrance is used to monitor the speed at the outlet when the Tesla valve is upstream and the speed and pressure change when the valve is upstream. The equivalent point Point4 is set in the first bend under the counter-current condition to monitor the velocity and pressure change trend of the fluid in the bend under the counter-current condition. The equivalent points Point5 and Point6 are set at the position near the exit of the second bend in the case of counter current, where a temporary cavitation phenomenon may occur. Point6 is set at the core of this low-speed area, and Point5 is located at the high-speed area of the exit of the bend.

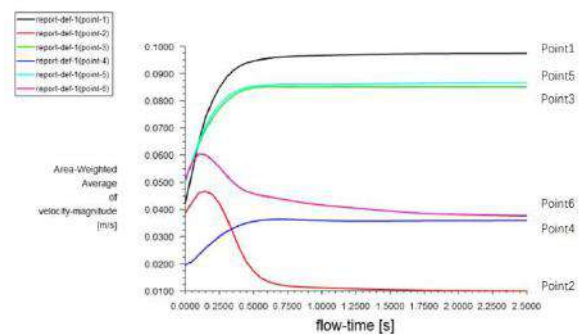


Fig. 3 test1 Reverse flow velocity variation diagram

As shown in Table 2, under the counter current condition of test1, the speed difference between Point1 and Point2 is the largest, which is consistent with the initial hypothesis. It can be seen from the figure that the speed of Point2 is close to stable after 1.5s, maintaining at 0.01m/s, while the speed of Point2 is finally maintained at 0.1m/s. The difference between the two is nearly 10 times, and the huge speed difference creates the possibility of cavitation.

Similarly, there is a large speed difference between Point5 and Point6, and the speed of Point4 does not change much. It only takes about 0.5s from the beginning to the final stabilization, which is similar to the stabilization time of Point1, Point5 and Point3. Both Point6 and Point2 are detection points located in the low-speed region. It can be seen that there is a fluctuation in the velocity within 0.025s, which is due to the sudden increase of the fluid velocity in the flow channel, resulting in the fluid velocity in these two low-speed regions being affected until the flow becomes stable. The speed slows down.

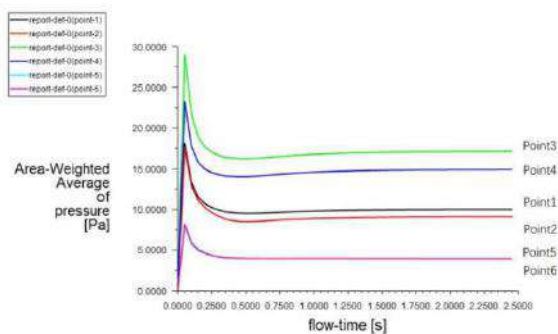


Fig. 4 test1 Reverse flow pressure variation diagram

As can be seen from Fig. 4, the pressure of the Tesla valve system is basically stable after 0.5s, Point3 is the monitoring point at the entrance, and the pressure is the largest. After the fluid enters the bend, the pressure of Point1 and Point2 is close, and the pressure of Point2 is slightly smaller, and the pressure in the cavitation core area is smaller than the surrounding pressure. The pressure of Point5 and Point6 is basically the same, and they are both the monitoring points at the counter current outlet. The pressure of these two points is the smallest or perhaps the difference is very small, which is not easy to see in the figure, and also indicates that the cavitation phenomenon here is not obvious. The counter current velocity pressure is basically stable after 0.75s, the flow of the fluid is basically unchanged, the vortex and cavitation phenomena exist at the same time, due to Angle reasons, the acceleration of the speed at the fluid junction is obvious, and the speed of the bend is basically the same as the inlet speed.

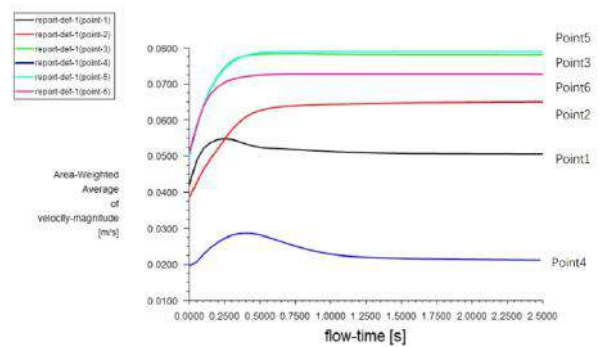


Fig. 5 test1 downstream velocity variation diagram

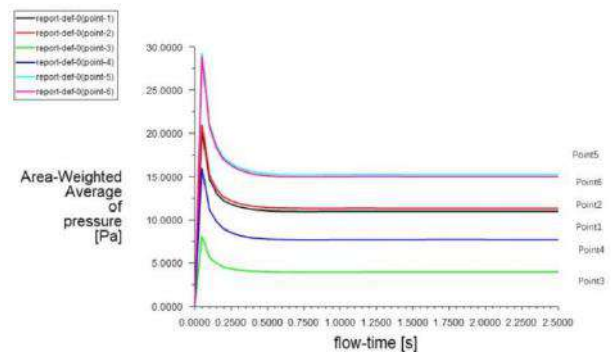


Fig. 6 test1 Up-flow pressure variation diagram

In the case of downflow, as shown in Figure 9, the speed of all monitoring points (except Point4) increases relative to the counterflow. As the monitoring point of the curve, the speed of Point4 is even lower relative to the counterflow, maintaining at about 0.02m/s after stabilization. It can be seen that in the downflow, the fluid does not flow into the curve as much as the counterflow. Point5 and Point6 as inlet monitoring points along the flow, the speed increases obviously. Point1 and Point2 are the monitoring points in the middle of the Tesla valve, and the speed increase is not large in the forward flow, at this time, most of the fluid flows in the straight channel, and the fluid in the bend is less, and the acceleration effect at the intersection is relatively small.

As can be seen from Figure 9, the pressure of similar monitoring points is very close, and the system begins to stabilize at 0.5s, which is much faster than the counter current situation. Only within 0.1s at the beginning, the pressure changes greatly, and the pressure is proportional to the distance from the upstream inlet. The highest pressure is close to 30Pa, and the maximum pressure after stability is about 15Pa. The minimum value is around 4Pa.

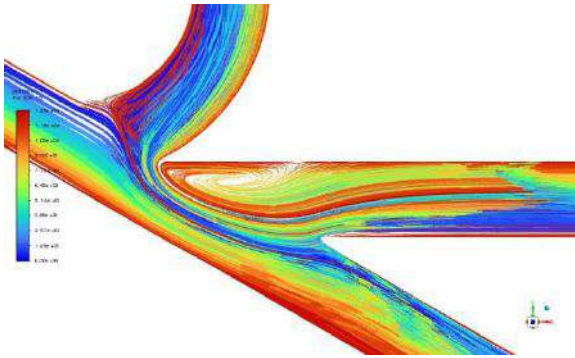


Fig. 7 test1 Particle trajectories at interchanges of counter current

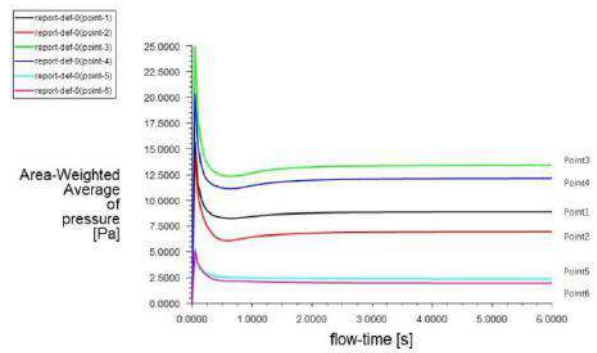


Fig. 9 test5 Reverse flow pressure variation diagram

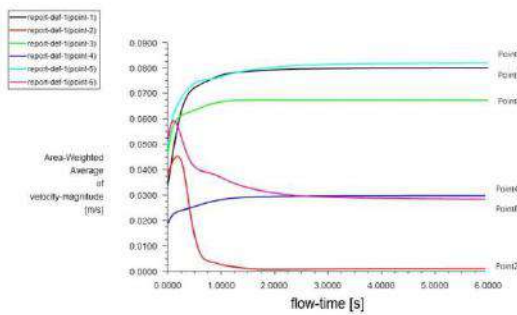


Fig. 8 test5 Reverse flow velocity variation diagram

As can be seen from Figure 8, the complexity of its speed change is much higher than that of test1, but there are still some similarities. For example, the speed difference between Point1 and Point2 is still very large, and the speed difference between Point5 and Point6 is slightly larger than that of test1. The speed of Point5 began to exceed the speed of Point1 after 1.5s, which was very close to the two. However, Point6, which was also in the low-speed area, did not slow down to 0 like Point1 and remained stable at about 0.028m/s. Combined with the speed cloud map, In theory, there should also be a zero-speed region in the low-speed region of Point6 like the middle interchange, which should be because the location of the point is not accurate. If it is really in the core of the low-speed region, the speed should be close to 0 after stability. The increase of the valve Angle and the increase of the flow channel section is beneficial to the stability of the flow of the Tesla valve.

As can be seen from Figure 9, the maximum pressure reaches 25Pa and is about 13Pa after stability. Compared with test1, which has a maximum value of close to 30Pa and a maximum value of 15Pa after stability, test5 has a lower system pressure, which indicates that test5 has a better system stability than test1.

Point3 is the inlet monitoring point in the case of counter current, the pressure is the highest, the pressure drops after the fluid enters the bend, and finally maintains around 12.5Pa. The pressure difference between Point1 and Point2 is about 2.5Pa, the pressure of Point5 and Point6 is very close to that of the surrounding area, and the pressure in the cavitation core area is smaller than that in the surrounding area. In the case of counter flow, the pressure at the end of the Tesla valve, Point5 and Point6, has decayed to a very low value. Therefore, there is no significant pressure difference between Point5 and Point6, so the probability of cavitation is very low, or the cavitation phenomenon is small and not obvious. The stabilizing time of the overall pressure is about 1s, which is a little slower than the 0.75s of test1. The increasing of the valve Angle and the size of the channel section may have adverse effects on the stabilizing time.

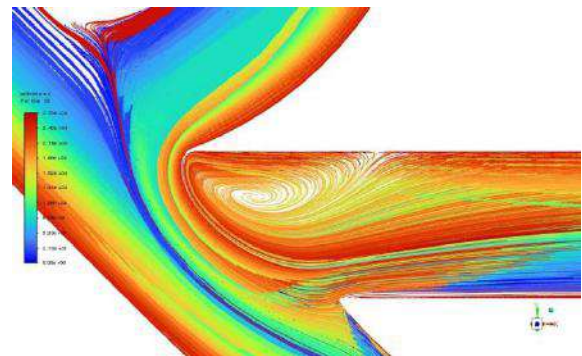


Fig. 13 test5 Particle trajectories at interchanges of counter current

Figure 10 shows that in the case of down flow, the speed of Point4 is the lowest, which is less than 0.02m/s after stability, indicating that in the case of down flow, only a small part of the fluid entering from the entrance flows into the bend, and most of it flows in the straight. Compared with the counter current situation, the speed of Point2 and Point6 both increased in the forward flow, and the speed of Point2 and Point3 was basically the same after

stabilization. Before 0.5s, Point1 and Point6 had a fluctuating stage, which first increased and then decreased. In the case of forward flow, the position of Point1 was close to the wall of the straight channel. When the fluid passed through the forward flow, it would impact the wall, and the speed increased for a short time, and then the speed decreased. Point6 is located at the upstream entrance, close to the side wall of the first bend. When the fluid flows through here, a small part of the fluid will enter the bend, resulting in speed attenuation. The speed attenuation of Point6 is larger than that of Point1. At the same position, the Point6 of test1 does not decay, but rises steadily and finally becomes stable. The position of Point6 is not affected by the Angle of the valve, indicating that the increase of the channel section will hinder the co-flow of the Tesla valve, resulting in the non-smooth co-flow.

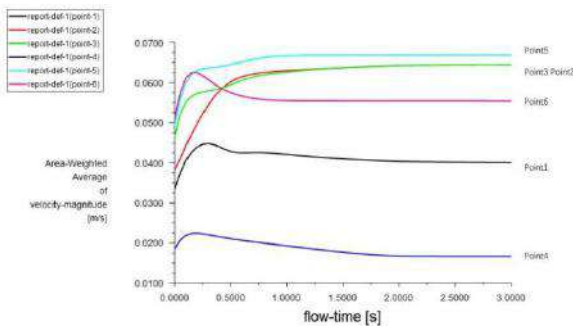


Fig. 10 test5 Up-flow velocity variation diagram

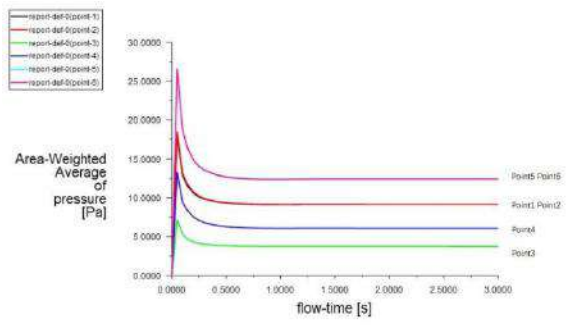


Fig. 11 Downstream pressure variation diagram

Figure 11 shows that the maximum pressure value of test5 is about 27Pa under the condition of downstream flow, and the final stable pressure is about 12Pa, with an intermediate fluctuation of about 15Pa. The minimum value appears at Point3. In the case of down-flow, Point3 is to monitor the pressure at the down-flow outlet, and its value is about 0.4Pa.

The pressure of Point5 and Point6, Point1 and Point2 are completely the same, and the changing trend is the same, indicating that there is no cavitation or vortex phenomenon in the straight channel under the condition of down flow.

The overall pressure of the system becomes stable after 0.5s, which is consistent with the situation of test1 downstream, and the pressure decreases in a step pattern with the distance of the velocity inlet.

4.2 Simulation verification of prediction results

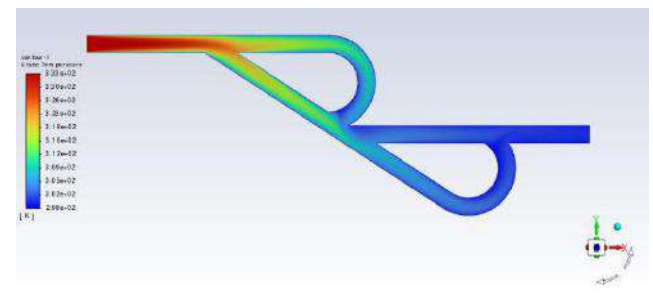


Fig. 12 Prediction group 1 counter current temperature cloud map

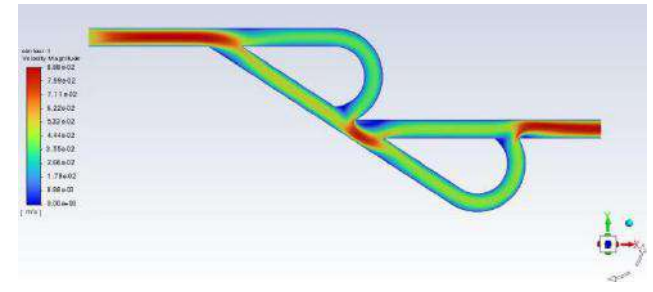


Fig. 13 Prediction group 1 countercurrent velocity cloud map

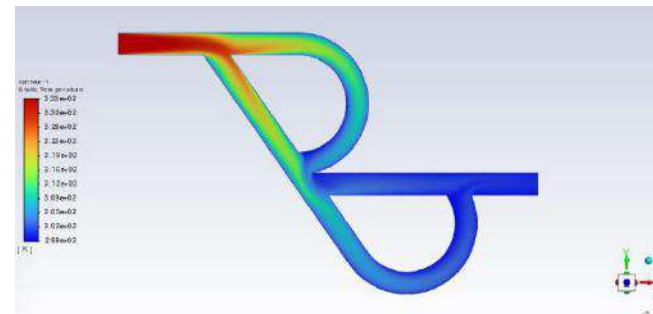


Fig. 14 Prediction group 5 counter current temperature cloud map

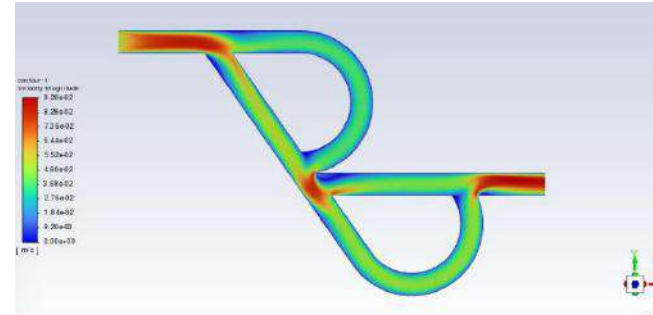


Fig. 15 Forecast group 5 counter current velocity cloud map

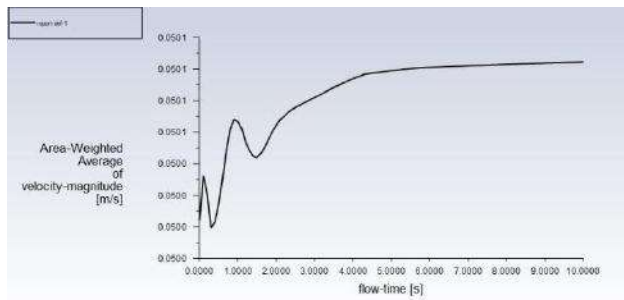


Fig. 16 Forecast group 5 velocity change at counter current outlet

Table 4 Simulation prediction parameter

Forecasting group	Downstream pressure drop ΔP/Pa	Countercurrent pressure drop ΔP/Pa	Downstream Nuf	Countercurrent Nur	Di	RP EC
YC1	18.24	19.79	383.87	399.32	1.1	1
YC5	16.57	18.04	272.28	289.17	1.1	1

The results obtained from the training of the neural network were verified. Two sets of data, YC1 and YC5, were selected for simulation verification, and the simulation results of the two sets of predicted data were obtained.

From the velocity and temperature cloud images, their flow conditions and temperature distribution are similar to the previous simulation results.

Combined with the above data, it can be seen that there are still some differences between the simulation data and the training results, and the simulation results are generally greater than the training results, indicating that the training model of the neural network is not as accurate as it is displayed, which may be due to too little training data or inappropriate hidden layers. Or the numerical solution method adopted by Fluent software, such as the finite volume method, is not suitable for discretization and numerical integration, and these steps will introduce certain errors. The selection and setting of numerical methods (such as grid resolution, time step, etc.) directly affect the accuracy of the simulation.

V. CONCLUSION

This research focuses on developing a trained neural network based prediction method to improve the prediction accuracy of the heat transfer mode of the Tesla valve heat sink. The unique design of the Tesla valve heat sink shows its advantages, but the traditional research methods face the problems of complicated calculation, time-consuming and inefficient. By comparing with traditional prediction methods, this study verifies the advantages of the proposed method in terms of calculation efficiency and prediction accuracy, and provides a new

possibility for the prediction of heat transfer mode of Tesla valve heat sink.

The results of two Fluent simulations show that the percentage difference of counter current Nu in YC1 is 49.26%, while that in YC5 is 40.93%. This indicates that the difference between the predicted value of YC1 and the simulated value of Fluent is slightly larger than that of YC5. The percentage difference of the Di parameter for YC1 is about 7.29%, while the percentage difference of the Di parameter for YC5 is about 1.43%.

This shows that on the Di parameter, the difference between the predicted value of YC5 and the simulated value of Fluent is smaller than that of YC1. The percentage difference of the RPEC parameters for YC1 is about 7.49%, while the percentage difference of the RPEC parameters for YC5 is about 0.82%. This shows that the difference between the predicted value of YC5 and the simulated value of Fluent is smaller than that of YC1 on the RPEC parameters.

The accuracy of the neural network training model under the known framework is sufficient, and its R value is very close to 1. However, in this study on the heat transfer of Tesla valve, the influence of valve Angle and cross section length on the heat transfer performance of Tesla valve is not a simple linear relationship. There are too few training data, and the differentiation of training data is not fine enough. The activation function or loss function used by the neural network is not suitable, which can lead to inaccurate prediction results. The flow and heat transfer process inside a Tesla valve can involve a variety of complex objects.

ACKNOWLEDGEMENTS

This work described in this paper was supported by the Research Funding of GDUP, Research on Lagrangian Coherent Structure Analysis of Heat Sink for heat transfer performance with Piezoelectric Fan, Special Project of Taishi Excellent Training Plan in 2024. Special Project of Science and Technology Innovation Strategy of Guangdong Provincial Department of Science and Technology in 2024, (Project No.: 2024A0505050022).

REFERENCES

- [1] Hu Zhuohuan, Ding Xiaoyu, Xu Jiayin. Effect of capillary core of Tesla Valve Channel Structure on start-up performance of loop heat pipe (2024). Advances in Chemical Engineering,
- [2] Cui Bowen. Research on Flexible Tesla Valve Micromixer with Unidirectional Flow Characteristics (2023), Northeast Dianli University, Jilin, China.
- [3] Thompson, S.M., Paudel, B.J., Jamal, T., et al. (2014)

- Numerical Investigation of Multistaged Tesla Valves. *Journal of Fluids Engineering*, 136, 081102-1-081102-9.
- [4] De Vries, S.F., Florea, D., Homburg, F.G.A., et al. (2017) Design and Operation of a Tesla-Type Valve for Pulsating Heat Pipes. *International Journal of Heat and Mass Transfer*, 105: 1-11.
- [5] De Vries, S.F., Florea, D., Homburg, F.G.A., et al. (2017) Design and Operation of a Tesla-Type Valve for Pulsating Heat Pipes. *International Journal of Heat and Mass Transfer*, 105: 1-11.
- [6] Qin Suhui. Finite-time and Fixed-time Stability Analysis of a Class of neural Networks (2022), Shanghai University of Finance and Economics, Shanghai, China.
- [7] Xun Kangdi, Li Xingcheng, Liu Kelei et al. Mobile phone graphite heat sink defect detection based on machine vision (2022). *Journal of Shaanxi University of Technology (Natural Science Edition)*.
- [8] Shen Yuanchu. Research on Multi-stability problems of several kinds of neural Networks (2022), Xuzhou, China University of Mining and Technology.
- [9] Wen Ting. Finite-time and Fixed-time synchronization analysis of several types of neural Networks (2022)., Huangshi, Hubei Normal University, China.
- [10] Ren Pu, Long Wei. Numerical analysis of Flow Field Characteristics and Cavitation formation Mechanism of Tesla Valve (2021). *Journal of Southwest University (Natural Science Edition)*
- [11] Qian Jinyuan, Chen Minrui, Li Xiaojuan et al. Numerical Study of Heat Sink Heat Transfer Enhancement in Tesla Valve Microchannels (2020) *Fluid Machinery*,
- [12] Qian Jinyuan, Chen Minrui, Li Xiaojuan et al. Numerical Study of Heat Sink Heat Transfer Enhancement in Tesla Valve Microchannels (2020) *Fluid Machinery*,
- [13] Zhou Runzhong, Qiao Yujie, Zhang Yuxiang et al. Simulation of Tesla Valve Performance (2020). *Physical experiments*
- [14] Wang Tao, Wang Haowen, Lin Yuchen, et al. Numerical Study on Hydraulic Cavitation of Tesla Valve (2020) *Journal of Chemical Engineering of Universities* 34
- [15] Feng Haojie. Dynamic Behavior Analysis and Application of Neural Networks (2020), Zhongyuan University of Technology, Zhengzhou, China
- [16] Zhang Xiaoling. Dynamic Analysis of Two Kinds of Neural Network Models (2020), Changsha University of Science and Technology, China
- [17] LIU Haiyang, Ma Jia, Wang Sen et al. Research on Single pilot Connectivity of Tesla Valves (2020). *Physics and Engineering* 120-124.

Afro-Womanism and the Development of Gender Consciousness

Dr Ibrahim Yekini¹, Armande M. Hounkpe²

¹English Department, University of Porto-Novo, Benin

Email: adebiaye20@gmail.com

²English Department, University of Abomey- Calavi, Benin

Email : hermande25@yahoo.fr

Received: 15 Aug 2024,

Receive in revised form: 11 Sep 2024,

Accepted: 16 Sep 2024,

Available online: 25 Sep 2024

©2024 The Author(s). Published by AI

Publication. This is an open-access article under
the CC BY license

(<https://creativecommons.org/licenses/by/4.0/>).

Keywords— *Afro-Womanism, Gender
Consciousness, Feminist Theory,
Intersectionality, Societal Norms.*

Abstract— *Afro-Womanism emerges as a critical framework that bridges the gap between traditional feminist thought and the lived experiences of Black women. By centering race, gender, and culture, Afro-Womanism provides a unique lens through which to explore both historical and contemporary gender issues. This article examines the evolution of gender consciousness through an Afro-Womanist lens, emphasizing the influence of societal norms on women of African descent. Through case studies from the 18th Century to the modern era, the article highlights how Afro-Womanism enables a more holistic understanding of gender dynamics across different cultural and socio-political contexts.*

I. INTRODUCTION

Afro-Womanism, a term introduced by Clenora Hudson-Weems in the late 20th century, offers a critical framework for centering the experiences of Black women within feminist discourse. Unlike mainstream feminism, which has often been critiqued for its focus on the struggles of white, middle-class women, Afro-Womanism recognizes the inextricable links between race, class, and gender in the lives of Black women (Hudson-Weems, 1993). It rejects the notion that the fight for gender equality can be fully understood without addressing the racial and economic factors that uniquely affect Black women. This approach not only broadens feminist theory but also challenges its traditional boundaries.

At its core, Afro-Womanism emphasizes community, family, and the cultural heritage of African women, distinguishing itself from the often-individualistic focus of Western feminist movements (Hudson-Weems, 1993). The inclusion of these elements provides a more holistic approach to addressing gender issues, highlighting the

importance of collective liberation over individual rights. By integrating intersectionality, a concept developed by Kimberlé Crenshaw (1989), Afro-Womanism recognizes the multiple layers of oppression that Black women face, particularly the ways in which societal norms intersect to shape their gendered experiences differently from white women.

In this article we explore the development of gender consciousness through the lens of Afro-Womanism, analyzing both historical and contemporary gender issues. By examining the societal norms that construct and impose gender roles, the article seeks to provide a nuanced understanding of how these roles affect Black women specifically. Through key Afro-Womanist principles and case studies, it will demonstrate how this framework enables a deeper exploration of gender dynamics, offering fresh insights into the ongoing discourse on gender equality.

II. THEORETICAL FOUNDATIONS OF AFRO-WOMANISM

Afro-Womanism represents a critical theoretical framework that redefines feminist discourse by centering the experiences and struggles of Black women. Developed by Clenora Hudson-Weems in the late 20th century, Afro-Womanism builds on several key theoretical foundations that distinguish it from other feminist frameworks. This section explores the theoretical underpinnings of Afro-Womanism, highlighting its unique contributions to understanding gender dynamics through the intersections of race, class, and gender.

Intersectionality and Race

A central tenet of Afro-Womanism is its integration of intersectionality, a concept pioneered by Kimberlé Crenshaw to elucidate how overlapping identities—such as race, gender, and class—interact to produce unique forms of oppression and privilege (Crenshaw, 1989). This framework is pivotal in understanding the multifaceted experiences of Black women, who navigate a complex matrix of racial and gendered discrimination. Afro-Womanism builds on this concept by highlighting how the intersection of these dimensions shapes the lived experiences of Black women in ways that cannot be fully comprehended through a singular focus on either race or gender alone (Crenshaw, 1991).

Crenshaw's work demonstrates that traditional feminist frameworks, which often emphasize gender in isolation, tend to overlook how race complicates and exacerbates gender-based oppression. For instance, Black women experience racial and gender discrimination simultaneously, which leads to compounded forms of oppression not addressed by mainstream feminist approaches (Crenshaw, 1989). This intersectional perspective reveals that Black women face unique challenges, such as racial stereotyping and gendered violence, which are not fully captured by analyses that consider race and gender separately.

Afro-Womanism incorporates intersectionality to advocate for a more nuanced analysis of these intersecting oppressions. By considering how race, gender, and class interact, Afro-Womanism calls for a feminist discourse that acknowledges and addresses these complexities. This approach not only provides a more comprehensive understanding of Black women's experiences but also challenges traditional feminist narratives that often exclude or marginalize these perspectives (Hudson-Weems, 1993). In doing so, Afro-Womanism pushes for a more inclusive and equitable feminist agenda that recognizes and responds to the intersecting forms of discrimination faced by Black women.

Critique of Mainstream Feminism

Afro-Womanism offers a critical analysis of mainstream feminist movements, highlighting their historical and ongoing limitations in addressing the experiences of women of color. Traditional feminist frameworks have often been criticized for their narrow focus on the struggles of white, middle-class women, thus marginalizing or ignoring the intersecting oppressions faced by women of color. This critique is evident in the works of early feminist figures such as Mary Wollstonecraft, whose seminal text, *A Vindication of the Rights of Woman* (1792), primarily addressed the rights and concerns of white, middle-class women, leaving out the compounded oppressions experienced by Black women and other women of color (Wollstonecraft, 1792).

Afro-Womanism, developed by Clenora Hudson-Weems, directly confronts this oversight by advocating for a more inclusive feminist discourse that recognizes and addresses the unique challenges faced by Black women (Hudson-Weems, 1993). This framework asserts that mainstream feminism's focus on gender as a singular axis of oppression is insufficient for understanding the complexities of Black women's experiences. Instead, Afro-Womanism calls for an analysis that integrates race, class, and gender to fully comprehend and address the multidimensional nature of Black women's struggles.

For example, mainstream feminist movements have frequently overlooked how systemic racism and economic disenfranchisement intersect with gender to exacerbate the oppression faced by Black women. This oversight has resulted in feminist strategies and policies that do not adequately address or alleviate the specific barriers faced by women of color (Collins, 2000). Afro-Womanism challenges traditional feminist narratives by emphasizing the need for a broader, more inclusive approach to gender justice that considers these intersecting oppressions. By advocating for this expanded perspective, Afro-Womanism seeks to ensure that all women's voices are heard and that their diverse experiences are recognized and addressed within feminist discourse.

Emphasis on Community and Spirituality

A crucial theoretical foundation of Afro-Womanism is its emphasis on the significance of family, community, and spirituality in the lives of Black women. This focus contrasts sharply with the individualistic tendencies of Western feminism, which often prioritizes personal achievement, autonomy, and self-reliance (Hooks, 1981). Afro-Womanism, on the other hand, acknowledges that Black women's experiences and identities are deeply intertwined with their communal and familial contexts. This framework asserts that understanding and addressing

gender issues requires an appreciation of these relational and collective aspects of Black women's lives.

In Afro-Womanism, family and community are not just social structures but vital sources of support, identity, and empowerment. This perspective highlights how communal bonds and spiritual practices are integral to Black women's resilience and well-being. For example, Afro-Womanism recognizes the role of extended family networks and community support systems in providing emotional and practical assistance, which can be crucial in navigating and resisting oppression (Collins, 2000). The communal aspect of Afro-Womanism also reflects a broader cultural emphasis on collective responsibility and mutual aid, contrasting with the often-solitary pursuit of personal goals in Western feminist thought.

Additionally, Afro-Womanism incorporates spirituality as a central component of empowerment and identity. Spiritual practices and beliefs often provide Black women with strength, purpose, and a sense of belonging that transcends individual challenges (Hudson-Weems, 1993). This approach underscores the importance of integrating spiritual and communal dimensions into discussions of gender justice, thereby offering a more holistic view of empowerment that acknowledges the interconnectedness of individuals within their communities.

By challenging the Western feminist focus on individualism and self-reliance, Afro-Womanism advocates for a more inclusive and supportive approach to gender justice. It recognizes that the well-being and empowerment of Black women are deeply connected to their familial, communal, and spiritual lives, and that addressing gender issues requires a comprehensive understanding of these relational aspects.

Historical Context and Legacy

Afro-Womanism draws deeply from the historical context of Black women's struggles and resilience to provide a comprehensive understanding of contemporary gender dynamics. This framework examines how historical systems of oppression, such as slavery and colonialism, have influenced and shaped the experiences of Black women over time. By acknowledging the historical roots of current issues, Afro-Womanism offers valuable insights into the continuity and evolution of Black women's experiences of oppression and resistance.

Enslaved Black women, for example, faced a dual burden of racial and gendered exploitation. Their labor, both in agricultural fields and domestic spheres, was essential to the economy of slavery. This exploitation was not merely an economic strategy but also a form of gendered violence specifically targeting Black women (Davis, 1983). Furthermore, their reproductive capacities were exploited to

increase the enslaved population, adding another layer of oppression that intersected with both race and gender. This historical context reveals how deeply embedded forms of discrimination have shaped the lived realities of Black women, laying the groundwork for ongoing marginalization.

Understanding these historical dimensions is crucial for addressing contemporary gender issues. Afro-Womanism situates current struggles within a broader historical framework, highlighting how historical injustices continue to affect Black women today. This perspective underscores that contemporary gender issues are not isolated phenomena but are deeply intertwined with historical processes of oppression and resistance.

By incorporating concepts such as intersectionality, critiquing mainstream feminist approaches, emphasizing the importance of community and spirituality, and contextualizing contemporary issues within historical frameworks, Afro-Womanism provides a nuanced and inclusive perspective on gender justice. This comprehensive approach not only enriches feminist discourse but also advocates for a more equitable and holistic framework for addressing the diverse experiences of Black women (Hudson-Weems, 1993; Collins, 2000).

In doing so, Afro-Womanism ensures that the complexities of Black women's experiences are acknowledged and addressed, promoting a more inclusive and informed understanding of gender dynamics.

III. HISTORICAL GENDER ISSUES: AN AFRO-WOMANIST PERSPECTIVE

This chapter delves into historical gender issues through the lens of Afro-Womanism, a framework that integrates race, class, and gender to offer a comprehensive understanding of Black women's experiences. Traditional feminist narratives often overlook the intersectional nature of oppression that affects Black women, focusing primarily on the struggles of white, middle-class women. In contrast, Afro-Womanism recognizes how colonial histories, racial dynamics, and socio-economic conditions uniquely shape the roles and rights of Black women (Collins, 2000). The exploration begins with the 18th century, a period marked by rigid patriarchal norms and Eurocentric ideals that profoundly influenced women's social positions and legal rights. While feminist thinkers such as Mary Wollstonecraft advanced arguments for women's rights, their analyses frequently neglected the compounded effects of race and class, leaving Black women's experiences largely unaddressed (Davis, 1983). Afro-Womanism fills this gap by examining how enslaved Black women faced dual

oppressions of gender and race, and how these intersecting factors were integral to their lived realities.

Moving into the post-emancipation era, the chapter highlights how societal norms continued to exploit Black women's race and gender to sustain their subjugation. Despite their significant contributions to social movements, Black women were marginalized both within mainstream feminist circles and Black liberation movements. Through figures like Sojourner Truth and Harriet Tubman, this chapter illustrates how Afro-Womanism reveals the nuanced ways in which Black women navigated and challenged these dual oppressions, advocating for a more inclusive and intersectional approach to gender equality (Collins, 2000). By applying an Afro-Womanist perspective, this chapter seeks to illuminate the complex historical landscape of gender issues and underscore the importance of recognizing the intersectional dimensions of oppression in feminist discourse.

The 18th Century and Early Gender Consciousness

In the 18th century, societal norms were heavily influenced by patriarchal and Eurocentric ideals, which profoundly shaped women's roles and rights. These norms established and reinforced rigid gender hierarchies, perpetuating the belief that women were inherently inferior to men. The prevailing patriarchal ideology dictated that women's primary roles were confined to domestic duties and submission, thereby limiting their opportunities for education, political involvement, and economic independence. Feminist pioneers such as Mary Wollstonecraft emerged as crucial voices challenging these oppressive structures. In her seminal work, *A Vindication of the Rights of Woman* (1792), Wollstonecraft advocated for women's education and argued for the fundamental equality of the sexes (Wollstonecraft, 1792). Her critiques of gender inequality were pioneering for their time, yet they predominantly focused on the experiences and rights of white, middle-class women, largely overlooking the compounded effects of race and class (Crenshaw, 1989).

Wollstonecraft's feminist arguments, while groundbreaking, failed to address the specific challenges faced by Black women, particularly those who were enslaved or colonized. Her work reflected the broader limitations of early feminist thought, which often marginalized the experiences of women of color. This omission left a significant gap in feminist discourse, as it did not consider how the intersections of race, gender, and class uniquely shaped Black women's experiences (Crenshaw, 1989). Afro-Womanism, as articulated by scholars like Clenora Hudson-Weems, addresses this gap by examining how race, class, and colonization uniquely shaped the experiences of Black women during this period

(Hudson-Weems, 1993). Unlike mainstream feminist approaches, Afro-Womanism integrates an understanding of the complex interplay between these factors, offering a more nuanced perspective on historical gender issues.

For instance, enslaved Black women in the Americas experienced dual oppression—both racial and gender-based. Their labor was critical to the economic system of slavery, with their contributions exploited in both agricultural and domestic spheres. They were subjected to severe working conditions, and their reproductive capacities were exploited to sustain and expand the enslaved population (Davis, 1983). This exploitation was not only a component of economic strategy but also a tool of gendered violence specifically targeting Black women. The dual oppression of Black women as both enslaved individuals and gendered beings underscores the necessity of an Afro-Womanist perspective. This framework illuminates how intersecting systems of race, gender, and class functioned within oppressive institutions like slavery, highlighting the limitations of early feminist movements in addressing the full spectrum of women's struggles (Collins, 2000).

Afro-Womanism in the Post-Emancipation Era

In the post-emancipation era, Black women continued to face systemic exploitation rooted in both race and gender, despite the significant political shift represented by the abolition of slavery. The end of legal slavery did not translate into immediate or comprehensive liberation for Black women. Instead, they remained marginalized within both mainstream feminist movements and Black liberation movements that emerged in the wake of emancipation. This period was characterized by a continued reinforcement of racial and gendered hierarchies, which were maintained through various societal norms and institutional practices (Collins, 2000).

Within the mainstream feminist movement, Black women were often sidelined. White feminist groups, while advocating for women's rights, primarily focused on issues pertinent to white, middle-class women and frequently excluded the experiences and needs of Black women (Collins, 2000). This exclusion was evident in the limited attention given to how race intersected with gender to compound the oppression faced by Black women. As a result, the feminist agenda of the time failed to address the unique struggles faced by Black women, reflecting a broader pattern of racial exclusion within feminist discourse. Similarly, in the Black liberation movements, male leadership often overshadowed the contributions of women. While these movements were crucial in fighting racial oppression, they frequently failed to address gender inequality within their ranks. Women's roles and contributions were undervalued, and their voices were

marginalized in the struggle for racial justice (Collins, 2000).

The Afro-Womanist perspective offers a critical lens for understanding how Black women navigated these dual oppressions. Afro-Womanism emphasizes the intersection of race and gender, providing a nuanced analysis of Black women's roles and contributions during this period. This framework reveals that Black women were not merely passive recipients of oppression but were actively engaged in shaping their own destinies and advocating for broader social change (Hudson-Weems, 1993). Afro-Womanism highlights the ways in which Black women asserted their agency, both within and outside of the formal political movements of the time.

Notable figures such as Sojourner Truth and Harriet Tubman exemplify the critical roles that Black women played in challenging and reshaping narratives around freedom and rights. Sojourner Truth's famous "Ain't I a Woman?" speech, delivered at the Women's Rights Convention in 1851, was a powerful indictment of both racial and gender-based discrimination. In her speech, Truth argued for the inclusion of Black women in the broader women's rights movement, challenging the prevailing assumptions about race and gender (Truth, 1851). Harriet Tubman, renowned for her role in the Underground Railroad, continued her activism post-emancipation by advocating for women's suffrage and civil rights. Tubman's post-war efforts demonstrated her commitment to both racial and gender justice, further highlighting the intersectional nature of her activism (Collins, 2000). These contributions underscore the importance of incorporating Afro-Womanist perspectives into historical analyses, enabling scholars to fully appreciate the complexity of Black women's struggles and achievements in the post-emancipation era.

IV. CONTEMPORARY GENDER ISSUES: AFRO-WOMANISM AND INTERSECTIONALITY

This chapter addresses contemporary gender issues through the frameworks of Afro-Womanism and intersectionality, offering a critical examination of how these perspectives illuminate the complex experiences of Black women in modern contexts. While historical analyses have underscored the intersections of race and gender that shape Black women's experiences, contemporary issues require an equally nuanced approach. In today's society, Black women continue to encounter multifaceted forms of oppression that cannot be fully understood through a singular lens.

Afro-Womanism, with its focus on the intersections of race, gender, and class, provides a valuable perspective for analyzing current gender dynamics. This framework

challenges both mainstream feminist and traditional liberation narratives by emphasizing the unique challenges Black women face and advocating for the centralization of their experiences in discussions of gender equality. By integrating an understanding of how systemic inequalities and societal structures impact Black women, Afro-Womanism reveals their ongoing struggles and resilience in contemporary settings.

Intersectionality, a concept developed by Kimberlé Crenshaw, complements Afro-Womanism by highlighting how overlapping identities—such as race, gender, sexuality, and class—interact to produce unique forms of discrimination and privilege (Crenshaw, 1989). This approach is crucial for addressing the complexities of contemporary gender issues, as it underscores the limitations of analyzing oppression through isolated categories. Intersectionality provides a comprehensive understanding of how multiple systems of power and discrimination intersect, shaping Black women's lived experiences in diverse ways.

By examining contemporary issues through these frameworks, this chapter aims to deepen the understanding of the challenges and opportunities facing Black women today. It explores how Afro-Womanism and intersectionality contribute to broader discussions of gender justice and social change, underscoring the importance of inclusive and intersectional approaches in addressing ongoing gender inequalities.

Modern Gender Consciousness

In contemporary gender discussions, Afro-Womanism offers an essential framework for analyzing the societal norms impacting Black women, offering insights often overlooked in mainstream feminist and civil rights narratives. Modern societal expectations continue to position Black women in roles emphasizing caregiving, community leadership, and nurturing, reflecting historical stereotypes rooted in slavery. The archetype of the "strong Black woman," for instance, both praises and burdens Black women, expecting resilience in the face of adversity while overlooking their struggles and needs (Hooks, 1981).

These societal pressures push Black women into managing both professional and personal responsibilities while contending with the compounded challenges of racial and gender discrimination. For example, Black women often experience a "double jeopardy" of discrimination—where their racial identity and gender are sources of systemic disadvantage. This intersectional oppression manifests in various ways, including disparities in income, healthcare, and educational opportunities, exacerbated by societal expectations that undervalue or ignore their contributions and struggles (Crenshaw, 1989).

Afro-Womanism highlights the contemporary invisibility of Black women within both feminist and civil rights narratives. While mainstream feminist discourse has traditionally centered on the experiences of white, middle-class women, and civil rights movements have focused on racial justice from a predominantly male perspective, Afro-Womanism underscores the necessity of including Black women's voices and experiences in these conversations (Hudson-Weems, 1993). This framework advocates for a more inclusive approach that recognizes the unique challenges Black women face and addresses their needs comprehensively.

Afro-Womanism also emphasizes the significance of family, spirituality, and community in Black women's lives, contrasting sharply with the often-individualistic focus of Western feminism. Western feminist approaches frequently prioritize individual achievement and autonomy, overlooking the collective and communal aspects of Black women's lives. In contrast, Afro-Womanism values the interconnectedness of family and community, recognizing that Black women's well-being and agency are deeply tied to their roles within these social structures (Collins, 2000). This emphasis on community and collective support challenges the notion of self-reliance prevalent in Western feminist thought and advocates for a more holistic understanding of empowerment, including communal and familial dimensions.

Additionally, Afro-Womanism critiques the narrow scope of Western feminist frameworks by addressing how systemic inequalities and societal norms shape Black women's experiences. It calls for a broader understanding of gender justice that incorporates the intersectional realities of race, class, and gender. This perspective is vital for addressing the ongoing challenges faced by Black women and ensuring that their needs and contributions are recognized within broader gender and social justice movements (Crenshaw, 1989; Hudson-Weems, 1993).

Afro-Womanism and the #MeToo Movement

The #MeToo movement, which has brought issues of sexual harassment and gender-based violence to the forefront, has faced criticism for centering predominantly on white women's experiences. While the movement has succeeded in highlighting the widespread problems of harassment and assault, Black women's experiences within this context are often overshadowed or marginalized. Afro-Womanism offers a crucial critique of this mainstream feminist focus, arguing that the movement has insufficiently addressed the intersecting impacts of sexism and racism that uniquely affect Black women.

Afro-Womanism, a framework developed to center Black women's experiences by integrating race, gender, and class,

provides valuable insights into the limitations of the #MeToo movement. Kimberlé Crenshaw's concept of intersectionality is pivotal, as it highlights how Black women experience compounded forms of discrimination that mainstream feminist discourse frequently overlooks (Crenshaw, 1991). Intersectionality emphasizes that issues of sexism and racism are interconnected, shaping the unique challenges Black women face. Black women are disproportionately targeted for sexual violence, yet their experiences are inadequately represented in discussions dominated by narratives from white women (Crenshaw, 1991).

Crenshaw argues that legal and social frameworks addressing sexual harassment and violence often fail to account for the compounded effects of race and gender, resulting in interventions that are less effective for Black women. These barriers, including racial stereotypes and systemic discrimination, perpetuate the marginalization of Black women's voices in mainstream feminist and #MeToo discussions (Crenshaw, 1991).

Furthermore, Patricia Hill Collins' concept of "Black Feminist Thought" reinforces the importance of considering the intersection of race and gender in feminist discourse. Collins argues that Black women's experiences are marginalized in feminist discussions because mainstream feminist frameworks have historically centered on the experiences of white, middle-class women (Collins, 2000). This historical exclusion has led to a limited understanding of the diverse experiences of women and hindered the development of more inclusive and effective feminist strategies.

Afro-Womanism critiques the mainstream #MeToo movement for its insufficient attention to these intersectional issues. It advocates for a more inclusive feminist movement that prioritizes marginalized groups' experiences, ensuring that all women's voices are represented and heard (Hudson-Weems, 1993). This approach calls for a shift from a singular, white-centered narrative to one embracing the diversity of women's experiences and challenges.

In conclusion, while the #MeToo movement has made significant strides in raising awareness about sexual harassment and violence, it has faced criticism for failing to fully address the intersectional realities of Black women's experiences. Afro-Womanism offers a critical perspective, highlighting the need for a more inclusive feminist discourse that centers the voices and experiences of marginalized groups. By incorporating insights from intersectional theorists such as Crenshaw, Collins, and others, the movement can better address the compounded

forms of discrimination faced by Black women and work toward a more equitable feminist agenda.

V. CONCLUSION

Afro-Womanism, developed by Clenora Hudson-Weems in the late 20th century, offers a comprehensive framework for analyzing gender consciousness through the intersections of race, class, and gender (Hudson-Weems, 1993). This approach addresses the shortcomings of mainstream feminist theories, which have historically prioritized the experiences of white, middle-class women while often neglecting the unique challenges faced by women of color. By focusing on the specific experiences of Black women, Afro-Womanism provides a more nuanced and inclusive understanding of gender issues, emphasizing the interconnected nature of various forms of oppression.

Central to Afro-Womanism is the recognition that race, class, and gender cannot be considered in isolation when examining the oppression of Black women. This framework critiques traditional feminist approaches that may prioritize gender issues without fully acknowledging the compounded impact of race and class. The concept of intersectionality is vital in Afro-Womanism, as it allows for a more comprehensive understanding of how societal norms and structures uniquely affect Black women, distinguishing their experiences from those of their white counterparts (Collins, 2000).

Afro-Womanism also critiques the historical oversight in feminist movements, where the focus on the rights of white, middle-class women often ignored the compounded oppressions of Black women. Figures like Mary Wollstonecraft, while pivotal in advocating for women's rights, did not account for the experiences of women of color, who faced both racial and gender-based discrimination (Wollstonecraft, 1792). Afro-Womanism pushes for a more inclusive historical and contemporary feminist discourse, highlighting the importance of community, family, and spirituality in the lives of Black women and calling for a broader understanding of gender justice (Hooks, 1981).

ACKNOWLEDGEMENTS

I extend my heartfelt gratitude to all who have supported me throughout this journey. Special thanks go to my advisor, Dr. Ibrahim Yekini, whose guidance, patience, and expertise have been essential in shaping this work. I am also deeply appreciative of my family and friends, whose unwavering support has given me strength, and to my parents for always believing in me and encouraging my ambitions.

I also want to acknowledge my colleagues and peers, whose feedback and camaraderie have enriched this process. Lastly, I express my gratitude to the scholars and activists whose work has inspired and informed my research. Your commitment to knowledge and social justice has been a guiding light in this endeavor.

REFERENCES

- [1] Collins, P. H. (2000). *Black Feminist Thought: Knowledge, Consciousness, and the Politics of Empowerment*. Routledge.
- [2] Crenshaw, K. (1989). *Demarginalizing the Intersection of Race and Sex: A Black Feminist Critique of Antidiscrimination Doctrine, Feminist Theory, and Antiracist Politics*. *University of Chicago Legal Forum*, 1989(1), 139-167. And (1991) *Mapping the Margins: Intersectionality, Identity Politics, and Violence Against Women of Color*. *Stanford Law Review*, 43(6), 1241–1299.
- [3] Hooks, B. (1981). *Ain't I a Woman: Black Women and Feminism*. South End Press.
- [4] Hudson-Weems, C. (1993). *Africana Womanism: Reclaiming Ourselves*. Bedford Publishers.
- [5] Truth, S. (1851). "Ain't I a Woman?" Speech delivered at the Women's Rights Convention, Akron, Ohio.
- [6] Wollstonecraft, M. (1792). *A Vindication of the Rights of Woman*

Simulation Study on Heat Transfer Conditions Based on Vertically Descending Evaporating Tubes

Guo-Xing Yang, Yan-Zuo Chang^{*}, Yan-Xiao Jia, Jin-Ping Chen, Shao-Bi Dai, Yu-Qiang Lin

Energy and Power Engineering, Guangdong University of Petrochem Technology (GDUPT), Maoming, 525000, China

*Corresponding author: 15839677372@163.com

Received: 19 Aug 2024,

Receive in revised form: 17 Sep 2024,

Accepted: 23 Sep 2024,

Available online: 30 Sep 2024

©2024 The Author(s). Published by AI Publication. This is an open-access article under the CC BY license

(<https://creativecommons.org/licenses/by/4.0/>).

Keywords— *biphasic flow, heat transfer conditions, numerical simulation, Vertical descending evaporation tube.*

Abstract— *This paper aims to investigate the heat transfer conditions of vertically descending evaporator tubes. Through numerical simulation methods, the flow patterns and heat transfer characteristics within the evaporator tubes under both uniform and abnormal heating conditions are analyzed. Fluent software is employed to simulate the normal evaporation process in uniformly heated evaporator tubes, exploring their gas circulation and local heat transfer conditions. Additionally, simulations are conducted for descending evaporator tubes under abnormal heating to analyze the impact of different heat distributions on the flow patterns and heat transfer within the tubes. The conclusion drawn is that the primary cause of working fluid descent in evaporator tubes is uneven heating of the tube bundle. A single evaporator tube forms a stable circulation, whereas an increase in the number of tubes in the bundle exacerbates the descent phenomenon. To prevent such occurrences, measures such as optimizing heat transfer, ensuring complete combustion, and regularly maintaining the pipelines can be implemented. Future research could further simulate real-world boiler heating conditions and explore the application of two-phase evaporation flow in other equipment.*

I. INTRODUCTION

At the 75th session of the United Nations General Assembly, the Chinese government pledged to enhance nationally determined contributions by adopting more robust policies and measures to strive for peaking carbon dioxide emissions before 2030 and achieving carbon neutrality before 2060. This policy aims to tackle global climate change, reduce greenhouse gas emissions, promote green development, and protect the ecological environment. Nowadays, energy issues have become a focal point of societal attention, and the proposal of the "dual carbon" goals poses a challenge to the expansion of traditional energy sources. The latest data shows that by the end of July 2024, China's total installed power generation capacity reached 31.0 billion kilowatts,

representing a year-on-year growth of 14%. Among this, solar power generation capacity was approximately 740 million kilowatts, up 49.8% year-on-year, while wind power generation capacity was around 470 million kilowatts, up 19.8% year-on-year. From January to July 2024, thermal power generation capacity totaled 14,106.1 billion kilowatts, a year-on-year increase of 3.5%. By the end of July 2024, thermal power's cumulative installed capacity accounted for 45.46% of the nation's total installed power generation capacity. The installed power generation capacity continues to grow, with wind and solar power exhibiting particularly strong momentum. However, despite the rapid development of renewable energy, given the current energy structure and actual demand, thermal power generation cannot be abruptly abandoned or significantly reduced in the short term. For some time to

come, thermal power will continue to play a crucial role in electricity supply, with its stable output capacity and mature technological system being indispensable for ensuring national energy security and stable economic operation.[1]

As a crucial pillar of thermal power generation, boilers are not only the starting point of energy and power conversion but also the core process of converting the chemical energy of fuel into internal energy. During combustion in the boiler, the fuel within the furnace releases a significant amount of heat. This heat is transferred to the water-cooled walls through radiation and convection, thereby facilitating the evaporation of water into steam.[2] During the operation of the boiler, heat continuously accumulates and transfers within the furnace. At this point, to achieve further energy conversion and utilization, evaporator tubes, a crucial component, are needed to convert water into steam. Evaporator tubes play a vital role in the boiler system, acting like an energy transmission channel that converts the heat generated by the boiler into powerful steam, providing continuous power support for subsequent power generation processes or other industrial applications.

The production of qualified steam by evaporator tubes is influenced by various factors, including working temperature, properties of the liquid working medium, flow rate and temperature of the supplied liquid, ambient humidity, stability of the heat source, internal structure of the heat tubes and liquid circulation status, external environmental temperature and pressure, as well as the design and manufacture of the evaporator tubes.[3] Additionally, evaporator tubes find extensive applications in numerous modern industrial sectors. For instance, in the paper industry, evaporators are used to concentrate pulp during the paper production process and to dry paper with steam, thereby producing high-quality paper products. In wastewater treatment, facilities such as urban wastewater treatment plants utilize evaporators to evaporate and recover water from wastewater, achieving the goals of water conservation and reducing wastewater discharge. In seawater desalination, evaporators are employed to evaporate seawater, removing salts and impurities to obtain usable freshwater.[4] In the solar energy sector, water is heated and converted into steam to generate electricity or achieve water cycle heating. With the development needs of modern industry, the performance of evaporators is continuously being improved to better meet the demands of various sectors.

Currently, it is observed that evaporation tubes experience heat transfer deterioration when subjected to excessive or insufficient heating. When the tube wall is heated with a constant heat flux, as the heat flux increases,

according to heat transfer theory, there exists a critical heat flux density for constant heat flux heating. At this point, the boiling states experienced by the water inside the tube include subcooled boiling and nucleate boiling. When the heat flux density on the tube wall exceeds the critical heat flux density, the boiling of the water inside transitions to film boiling. At this stage, due to the increased presence of gas near the tube wall, heat transfer becomes less efficient than in the previous stage, causing the wall temperature to rise rapidly. If boiling continues, when it reaches the mist stage, the adhering water film is evaporated, and the excessive gas once again leads to heat transfer deterioration.[5] On the other hand, insufficient heating issues caused by various factors such as combustion or structure are also relatively common. These issues are mainly manifested as heat discrepancies between the water-cooled walls or among the evaporator tube bundles. In particular, evaporator tubes that are less heated may experience circulation stagnation, free water levels, and reverse circulation.[6] For many riser tubes in the boiler's evaporation water cycle, the heat they receive is not entirely uniform but rather uneven. When uneven heating occurs, the amount of steam generated and the temperature within the tubes due to heating also become uneven, leading to uneven pressure distribution and subsequently uneven flow velocities within the tubes. When this uneven heating reaches a certain level, circulation stagnation or even reverse flow phenomena may occur, and for horizontally placed tubes, steam-water stratification may arise.[7]

Currently, research on fluid flow in pipes has become a hot topic, encompassing aspects such as fluid flow patterns and heat transfer conditions. However, most studies focus on the flow and heat transfer of fluids in horizontal pipes, while research on vertical pipes is relatively scarce, especially regarding heat transfer in vertical pipes under uniform heating boundary conditions. Typically, analyses of fluid heat transfer in vertical pipes are predominantly based on single-phase fluid studies, whereas research on multiphase fluids mostly remains confined to horizontal pipes.[8] For instance, the flow of refrigerant working medium in air conditioning evaporators and the condensation process of refrigerant vapor in horizontal heat exchange tubes in condensers are relevant examples. The reverse flow caused by uneven heating of evaporator tubes poses significant obstacles to the normal operation of the boiler's water cycle and its daily work. In practice, this issue has been addressed through actual experimentation, but there is still limited research exploring this problem from a simulation perspective.

The research approach in this paper starts with real-world problems, integrating knowledge from heat transfer,

fluid mechanics, and boiler principles. Utilizing the Fluent module in ANSYS 2022 R1 for simulations, it will explore the vapor-liquid two-phase fluid flow patterns in evaporator tubes experiencing insufficient heating and the development of descending flows. Additionally, the relationship between heat flux density and thermal conductivity will be considered.

II. INTRODUCTION TO THE MAIN MODELS

The evaporation tubes, steam drum, downcomers, headers, and connecting pipes in the boiler evaporation equipment were selected for modeling. The model was simplified primarily with reference to the relevant chapters on natural water circulation in textbooks on power plant boiler principles, in order to highlight the key research objects. Simplified models were created for the evaporator tube bundles, steam drum, downcomers, and headers. For example, only the pipe models were depicted for the evaporator tube bundles, which were assumed to be of the plain tube type, and most of the other structures and internal steam-water separation structures in the steam drum were omitted. The following figure provides a rough conceptual illustration of the geometric modeling:

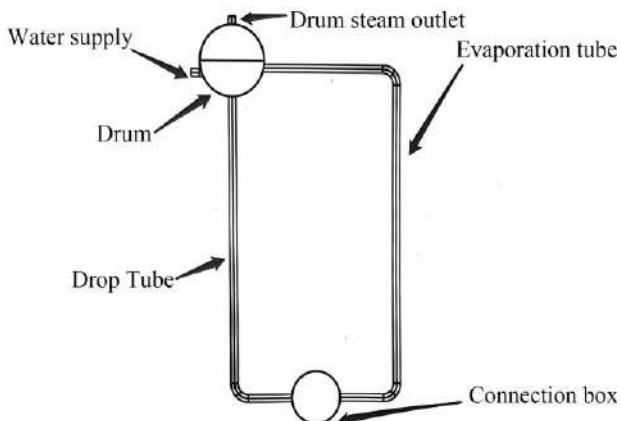


Fig.1: Roughness diagram of geometric modeling

III. SIMULATION OF WORKING FLUID FLOW IN A UNIFORMLY HEATED EVAPORATOR TUBE

3.1 Simulation of normal evaporation in a uniformly heated evaporator

Before further investigating the abnormal conditions of the evaporator tubes, the normal evaporation water cycle was first simulated. A single tube was selected for the simulation, with the middle section cross-section observed to examine the flow patterns inside the tube. Additionally, this study falls under the category of unsteady-state research. For multiphase flow, the Mixture

model was chosen in this study based on the fluid properties of boiling heat transfer within the tube.

The uniformly heated evaporator tube circulation system was considered as an open system with mass and energy exchanges with the outside environment. The mass inlet was the water supplied by the feedwater pump, which was delivered to the lower inlet of the steam drum. The corresponding inlet in the model was set as a mass flow inlet with a mass flow rate of 300 kg/m^3 . Since the water from the feedwater pump passes through the deaerator and economizer, it has a higher temperature, and the mass flow inlet temperature was set at 50°C . The mass flow outlet was the steam discharged from the upper outlet of the steam drum. The steam discharged from the steam drum needs to pass through the superheater and reheater to meet specified requirements before entering the turbine. Therefore, a pressure outlet was set at the outlet surface of the steam drum in the model. The pressure outlet boundary condition defined the static pressure at the outlet boundary of the flow field. The static pressure value was used when the flow field was subsonic, while the pressure was interpolated from within the flow field when the outlet reached supersonic speeds. The backflow conditions were set as close as possible to reality to ensure the convergence of the calculation. For heat input, due to the uniform heating of the evaporator tube, a constant heat flux density was directly set using the wall condition in the boundary conditions. Based on the data, the specific heat value for the single evaporator tube wall in this simulation was $10,000 \text{ W/m}^2$.

3.2 Solve and calculate

For the discretization scheme, Fluent solves the governing equations of the flow field to obtain the values of flow variables at all control points. The method used in the computation process for this solution is the QUICK (Quadratic Upwind Interpolation for Convective Kinematics) scheme. The QUICK scheme provides values at boundary points using a mixed form of weighting and interpolation. The QUICK scheme was originally proposed for structured grids (i.e., quadrilateral grids in two-dimensional problems and hexahedral grids in three-dimensional problems), but in Fluent, the QUICK scheme option can also be used for unstructured grid calculations. In unstructured grid calculations, if the QUICK scheme is selected, the values at non-hexahedral (or non-quadrilateral) edge points are computed using the second-order upwind scheme. The QUICK scheme offers higher accuracy when the flow direction aligns with the grid orientation. Therefore, the QUICK scheme was chosen for this study.[9][10]

Since the upper half of the steam drum contains a constant presence of gas, local initialization is required. A specific grid region within the steam drum (which has been previously meshed) was selected, and by setting the gas volume fraction to 1, it was maintained as a gaseous region.

IV. SIMULATION OF A DESCENDING EVAPORATOR TUBE UNDER ABNORMAL HEATING

My main objective is to simulate the occurrence of reverse flow in a uniformly heated evaporator tube using numerical simulation methods and compare it with the normal circulation flow conditions. Through simulation, I aim to seek answers to the problem of reverse flow in the evaporator tube. The working conditions inside a uniformly heated evaporator tube under normal circumstances have already been determined. The next step is to conduct a simulation analysis of abnormal conditions with uneven heating. The geometric model used here is the previously mentioned evaporator tube bundle consisting of three tubes, and a preliminary comparison of the flow patterns in the evaporator tube during descent under abnormal conditions with those under normal conditions will be made. To better represent abnormal conditions, a subsequent simulation using an evaporator tube bundle consisting of 10 tubes will be conducted.

In the three-tube model, the mesh size for the lower part of the steam drum and the header is relatively large, approximately 0.01. Since the evaporator tube is the focus of the study, a smaller mesh size of about 0.001 is used for division. For the gas part of the steam drum, the unit mesh size is about 0.002. The remaining non-critical components adopt automatic mesh generation by the system to save space and reduce equipment pressure. Ultimately, the number of mesh elements in this model is approximately 650,000.

When entering the Fluent solver, the environment settings, solver configuration, solution method, relaxation factors, and initialization are the same as those for the single-tube model. However, the boundary condition settings are different. For the three-tube model, the boundary conditions that need to be adjusted include the mass flow rate at the system inlet and the heat received by each tube. The solution settings and initialization remain consistent with those used previously.

4.1 Simulation results

The following is a nephogram of the results of the three evaporation tubes:

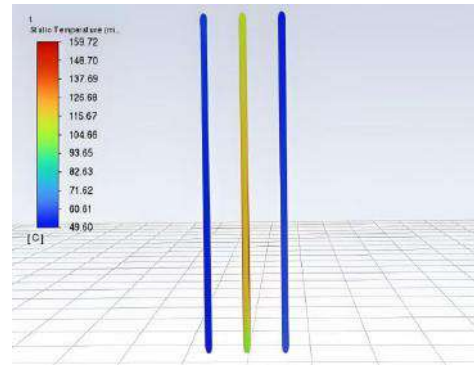


Fig. 2: Profile temperature nephogram of three root canals

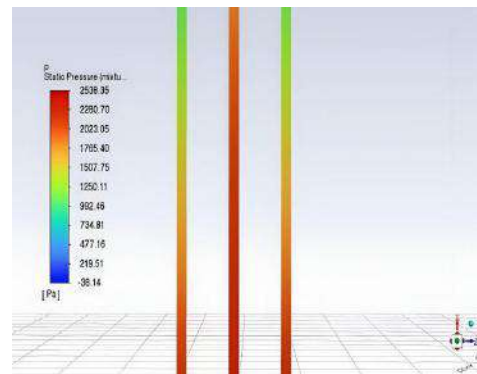


Fig. 3: Profile pressure nephogram of three root canals

4.2 Simulation results of three-tube model with different heat distribution

For the phenomenon of descending evaporator tubes, due to variations in uneven heating of the evaporator tubes, different heat distributions will be used to simulate as many scenarios as possible, in order to obtain more diverse patterns for convenient comparison and summarization. The following are the boundary conditions:

Table.1: The setting of boundary conditions for each tube:

Example	Heat of the first tube	Heat of second root canal	Third root canal heat	Inlet flow of water supply
Case1	18000w	8000w	5000w	400L/m ² .s
Case2	12000w	12000w	6000w	400L/m ² .s
Case3	8000w	8000w	5000w	400L/m ² .s

The simulation results are shown below

Case 1: 1.8W heat + 0.8W heat + 0.5W heat, with a water flow rate of 400L/m².s

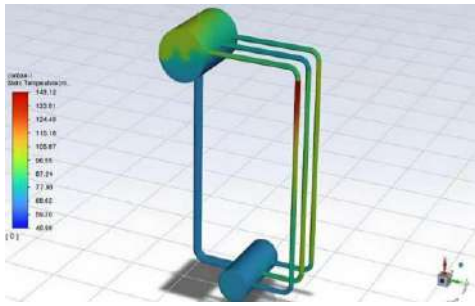


Fig. 4: Temperature nephogram

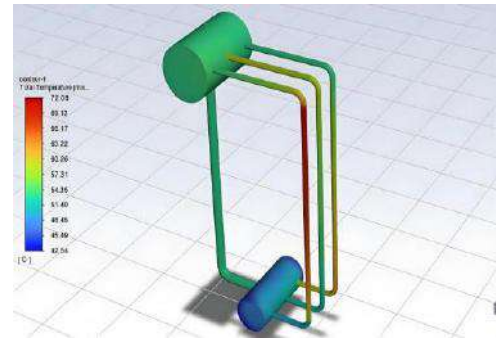


Fig. 8: Temperature nephogram

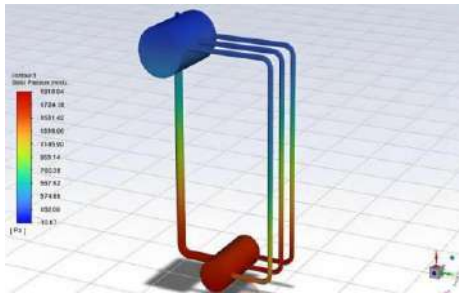


Fig. 5: Pressure nephogram

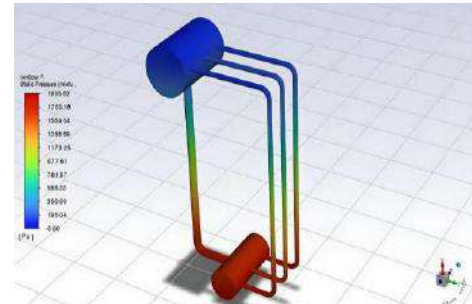


Fig. 8: Pressure nephogram

Case 2: The first two have a heat output of 1.2W, and the last one has a heat output of 0.5W, with a water flow rate of 450L/m².s.

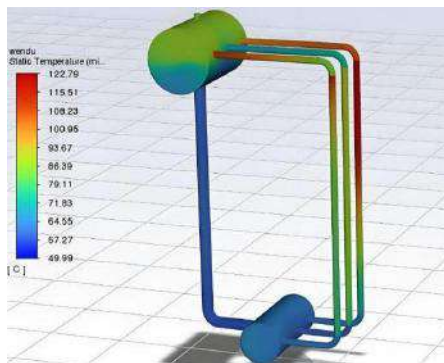


Fig. 6: Temperature nephogram

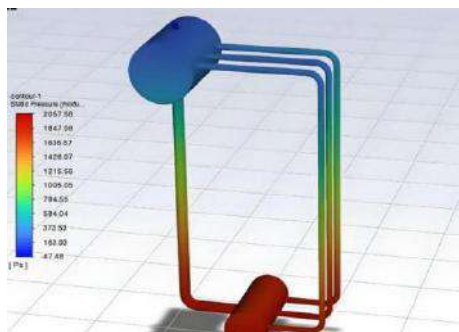


Fig. 7: Pressure nephogram

Case 3: The first two have a heat output of 1.0W, and the last one has a heat output of 0.7W, with a water flow rate of 400L/m².s.

4.3 Simulation of descending evaporator tubes in a ten-evaporator tube bundle

To better represent the uneven heating of evaporator tube bundles in reality, a model with ten tubes is used for simulation. First, a simulation of uniform heating is conducted, assuming that each tube receives the same amount of heat to achieve normal heating results. The mass inlet is set to 700kg/m².s, and the pressure outlet is set to a pressure reflux of 99 degrees Celsius. The boundary conditions for wall temperature heating are the same as before. A simulation of uneven heating of the ten tubes is then conducted, with other settings remaining the same as above, except for different boundary conditions.

In this scenario, the flow rate for all ten tubes is set to 700kg per square second. The heat input for the first tube is 6000w, while the heat input for the second to the ninth tubes is 12000w. Specifically, the heat input for the tenth tube is set to 10000w.

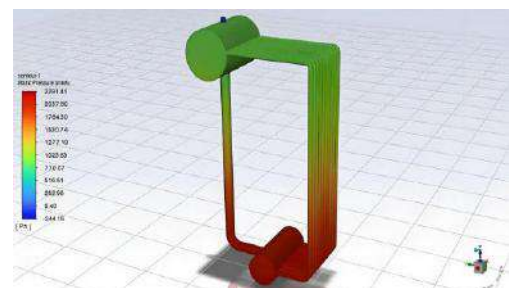


Fig. 9: Pressure nephogram of uneven heating in a ten-tube configuration

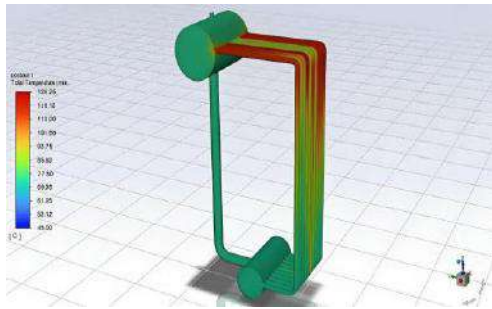


Fig. 10: Temperature nephogram of uneven heating in a ten-tube configuration

It can be observed that in cases of uneven heating, if the water level in the boiler drum is too low, or if there are significant fluctuations or excessively low water levels, it can lead to the formation of a vortex funnel at the inlet of the downcomer. This vortex funnel can "draw in" steam into the downcomer, which reduces the density of the working fluid in the downcomer and subsequently lowers the circulation head.

V. SIMULATION RESULTS AND DISCUSSION

For the two-phase flow of steam and water in the downcomer, the single-phase water velocity distribution in the cross-section of the vertically ascending tube is highly uneven. Specifically, the water near the wall flows slower due to the effect of water viscosity, while the water at the center of the tube flows fastest. When water near the tube wall absorbs heat and generates bubbles, these bubbles are propelled upwards by buoyancy, causing them to move faster than the water. The bubbles close to the wall, influenced by the slower flowing water nearby and the faster flowing water at the center of the tube, will migrate towards the center, resulting in the bubbles, like the water, moving faster at the center than at the edges.[11] This phenomenon is attributed to the combined effects of buoyancy and water flow. If either of these two forces produces a different effect—for instance, if the water flow direction is reversed—then, following the same principle, the water flow would be ahead of the bubbles. These slower-moving bubbles would also be pushed away from the center of the pipe under the influence of the swirling flow.

(1)The Nusselt number calculation equation at this time is:

$$Nu = 0.023Re^{0.8} Pr^{0.4} \left(\frac{n_f}{n_w} \right)^{0.11} \quad (1)$$

Where Re is the Reynolds number, and the characteristic radius is the radius of the heated evaporation

tube (22); Pr is the Prandtl number; n_f , n_w represents the viscosity of the fluid and the wall.

As the water near the tube wall absorbs heat and its temperature rises to the saturation temperature, local bubbles are generated. However, much of the water has not yet reached the corresponding temperature, resulting in subcooled nucleate boiling at this stage.[12] When all the water in the tube has absorbed heat from the tube wall, it enters the second stage of boiling heat transfer—nucleate boiling. At this point, bubbles gather at the center of the tube to form steam slugs, which are separated by layers of water. As the water between the steam slugs absorbs more heat and evaporates during its upward journey, the steam slugs merge into a ring-shaped formation around the tube. Subsequently, the fluid inside the tube further absorbs heat, and the water film left on the wall due to viscosity also turns into gas. At this stage, the steam appears as a mist, which still contains moisture and can continue to absorb heat until the last trace of water vapor disappears, and the steam inside the tube becomes a single-phase fluid again.

The simulation results for a normally operating, uniformly heated evaporation tube are as follows:

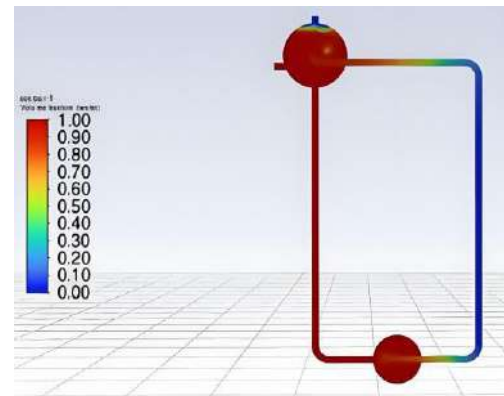


Fig. 11: Volume fraction nephogram of uniformly heated tube

As can be seen, after the evaporation tube on the right side is heated and generates gas, the gas initially flows up and down without forming a circulation. When the conditions are met, the fluid (gas) with a smaller volume fraction in the evaporation tube begins to flow upward, while the red fluid (water) on the left flows downward through the header and towards the heated tube. At this point, the gas in the evaporation tube rises to the steam dome, and the gas-liquid interface remains at a stable position. The flow pattern analysis inside the evaporation tube is similar to the data for uniformly heated tubes.

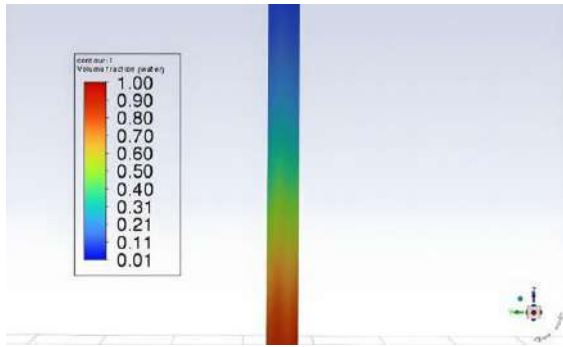


Fig. 12: Water volume fraction distribution diagram for a uniformly heated tube

As can be seen, for a normally operating, uniformly heated evaporation tube, the water volume fraction nephogram shows a distribution from 100% inside the tube to 0.01% at the top of the tube, which is quite consistent with this situation. Of course, for the superheated steam mentioned above, in the boiler water process, it needs to leave the steam dome and pass through the reheater and superheater for further heating before it can become the superheated steam required by the steam turbine.

This process can also be analyzed in engineering thermodynamics. When unsaturated water that has not reached the saturation temperature at the corresponding pressure is heated, the thermal motion of the water molecules intensifies, the temperature rises; and the specific volume increases. When the saturation temperature is reached, the water begins to vaporize, with the saturation pressure and temperature remaining constant. If heating continues, the amount of water decreases, the amount of gas increases further, and the water volume fraction decreases as it moves upward until it all turns into water vapor. At this point, the steam is called dry saturated steam. If this steam is further heated into the superheated stage, the heat absorbed at this time is superheat. However, since the inside of the tube is all gas, heat transfer is not as efficient as it was with the previous liquid, which can cause the wall temperature to rise rapidly, potentially damaging the equipment. Finally, the dry saturated steam absorbs heat, and its temperature exceeds the saturation temperature, becoming superheated steam.

From the temperature contour plot, it can be observed that the temperature continuously increases as heat is absorbed from the bottom to the top of the tube, reaching its peak as steam at the final stage. The temperature at the topmost part can reach close to 200 degrees Celsius, indicating that the gas there is likely superheated steam. Comparing it with the volume fraction plot, it is found that the water volume fraction at the corresponding position is 0, confirming it as superheated steam. If the water volume

fraction is not exactly 0 but close to 0, it is highly likely that there is still a partial water film present. If the tube is completely filled with gas, the heat loss and thermal damage to the tube wall can be severe. The enormous heat cannot be promptly absorbed by the working fluid, leading to deterioration of the tube's performance and potential harm to the equipment.[13]

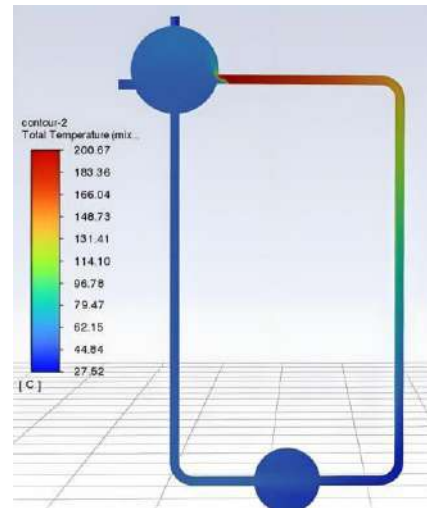


Fig. 13: Temperature nephogram of a uniformly heated tube

Under normal conditions, as previously mentioned, the flow pattern distribution from the bottom to the top of the tube is as follows: single-phase liquid → bubbly flow → slug flow → annular flow → single-phase gas.[14][15] The surface heat transfer coefficient during this process should first increase and then decrease. Specifically, it increases continuously from liquid convection heat transfer to annular flow. When it reaches single-phase gas flow, the liquid film on the tube wall completely evaporates, leaving only gas in contact with the tube wall. The thermal conductivity (Nu) of gas is relatively smaller than that of liquid. Therefore, when the difference in Nu is not significant, the surface heat transfer coefficient is smaller than that of gas.

Next, we simulate a descending evaporation tube with uneven heat transfer. From the temperature nephogram, it is clearly visible that the second tube is filled with steam and has a higher temperature than the other two tubes, reaching 150°C, which is consistent with the volume fraction nephogram showing that it is mostly steam. The temperature of the first tube is about 80°C. From the volume fraction nephogram, it can be seen that it is heated well, with some steam already entering the steam dome. At this time, most of the fluid inside the tube is subcooled water, resulting in a lower temperature. The third tube is significantly underheated (4000W), with much of the

water inside the tube not reaching the saturation temperature due to insufficient heat absorption. The overall temperature of this tube is lower than the first two and close to the temperature inside the descending tube, indicating severe underheating.

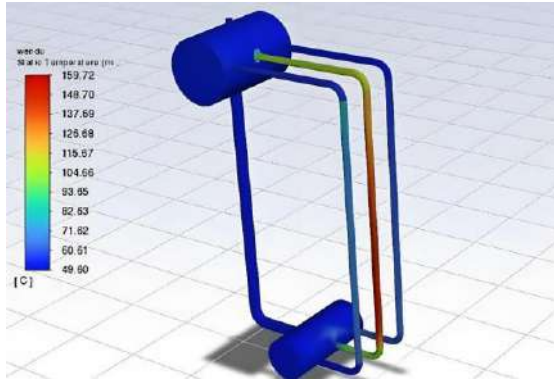


Fig. 14: Temperature nephogram of an abnormally heated evaporation tube

Due to the different heat reception conditions of the evaporation tubes, the most directly affected are the non-flowing working fluids inside each tube. Therefore, in the post-processing of this simulation, a sectioning method is adopted to analyze the evaporation tubes with different heat reception conditions through the sectioning of nephograms.

Firstly, let's analyze the evaporation tube with a heat reception of 15000W. As shown in the figure, it is the first tube from the top. From the figure, it can be seen that starting from the bottom of the evaporation tube (from left to right), there is initially forced convection heat transfer between the liquid and the tube wall. Subsequently, as the water temperature rises to the saturation temperature, bubbles are generated, and the water volume fraction begins to decrease to the range of 0.8 - 0.9. Then, with further heating of the tube wall, the gas inside the tube gradually increases, which is basically in line with the flow pattern of a normally heated evaporation tube.

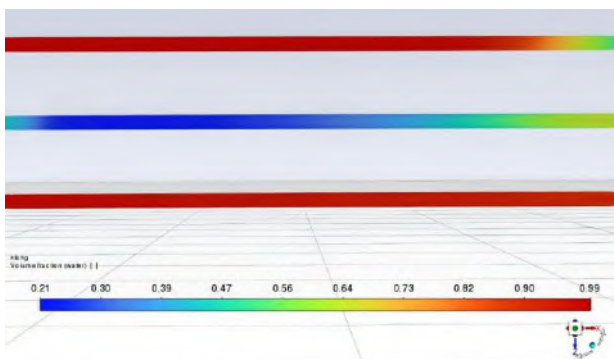


Fig. 15: Sectional volume fraction of three tubes with uneven heat distribution

Secondly, for the second tube, it can be seen from the volume fraction diagram that the gas content is higher near the tube wall. The water flow at the upper part of the tube (as shown on the right side of the figure) has not yet vaporized and is still in a liquid state. From this, it can be inferred that the liquid here is flowing downwards. The downward-flowing liquid will also generate gas after being heated by the tube wall, but the gas is carried downwards, causing a large accumulation of gas at the bottom of the tube. If the pressure here is greater than the pressure in the descending tube, the gas will enter the header.

At the same time, from the perspective of pressure, the pressure in the second tube is generally higher than that in the first and third tubes. This is because there is a large amount of steam flowing downwards in the second tube at this time. Due to insufficient heating, the working fluid in the third tube remains in a liquid state, and the pressure is relatively stable.

When there is a downward flow of heat in the evaporation tube, due to the upward buoyant force on the vapor bubbles, the vapor bubbles will only be carried downwards when the water velocity is greater than the upward floating velocity of the vapor bubbles.[16] Therefore, the flow pattern of downward water flow in the evaporation tube caused by uneven heat distribution, especially the flow pattern changes occurring during the downward flow process, will be influenced by the bubble velocity and water flow velocity. In view of this, the article presents the velocity nephogram of the simulation below.

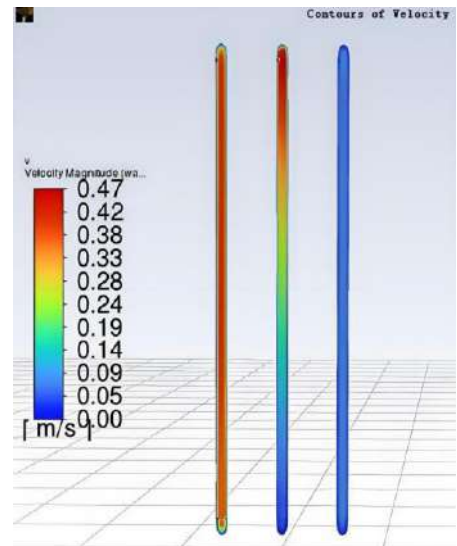


Fig. 15: Liquid velocity in the three tubes

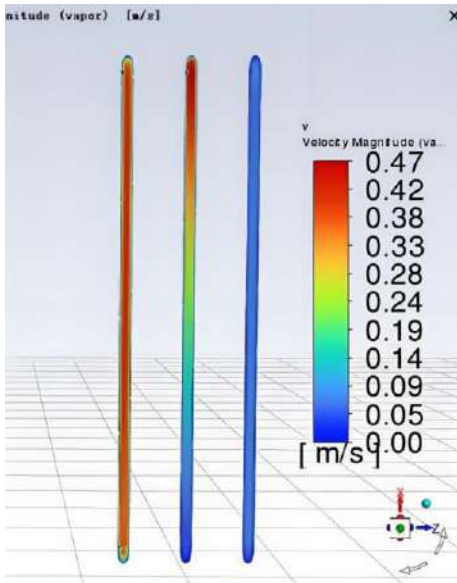


Fig. 16: Gas velocity in the three tubes

The sections of the first, second, and third tubes are shown from top to bottom in the figure. It is clearly visible from the figure that due to the scarcity of liquid and abundance of gas in the second tube, there is more liquid in the first and third tubes.

$$h = \frac{N_{\mu} \lambda}{d} \quad (2)$$

Furthermore, considering that the thermal conductivity of liquids is greater than that of gases, it can be inferred that when Nu is the same (the expression for Nu is the same for boiling heating inside the tubes), the surface convection coefficient of gases is larger than that of liquids. Therefore, the overall heat transfer rate is not as good as in the first three tubes, and the heat transfer efficiency of the second tube is very low.

After the previous comparisons, we have contrasted several heat transfer conditions of evaporation tubes under normal and abnormal operating conditions, and also conducted a simple flow pattern analysis incorporating knowledge of two-phase flow.

For normal heat reception, the heat received by each tube is consistent. Due to uniform heat reception, the flow patterns and distribution of state parameters within the uniformly heated tubes are similar. The main manifestations are: the heated liquid water within the tube with uniform heat flux density gradually produces steam after subcooled boiling and nucleate boiling. The bubbles rise under the influence of buoyancy and viscous forces. The upward steam is still heated by the wall heat flux, but the heating conditions are different. This is mainly manifested by the presence of gas-liquid mixture at the

bottom and mostly gas at the top, which causes the upper part of the gas to gradually heat up and eventually become superheated steam under heating.

For the situation caused by abnormal heat reception, the first reason is that the excessive difference in heat reception among the evaporation tube bundle leads to excessive pressure in the tubes, causing uneven pressure and resulting in the downward flow of water in some tubes under the influence of pressure. This part of the tubes flowing downward will still undergo the aforementioned boiling stages under uniform wall temperature heating, transitioning from liquid to gas. Finally, the downward-moving gas appears in the lower header. The difference from the above is that during the downward process, bubbles generated when the water is heated to saturation temperature move upward under the influence of buoyancy and gravity. However, the water flow direction at this time is opposite to the normal situation, so the direction of bubble movement is inconsistent with the normal situation.

For the abnormal situation where the reverse flow of steam caused by uneven heat reception in the evaporation tubes is heated and moves downward, the main reasons are uneven heat reception in the evaporation tubes, excessive resistance in the descending tubes, and excessive pressure changes. Measures can be taken from both structural and operational aspects.[17]

Structural measures include: (1) Dividing the circulation loops based on heat reception conditions; (2) Improving the heat reception conditions of the tubes at the four corners of the furnace; (3) Enhancing heat transfer by adding structures such as fins and using threaded tubes; (4) Adopting a simple layout for large-diameter descending tubes to minimize stress on the piping.

Operational measures that can be implemented include: (1) Selecting a larger ratio of descending tube cross-sectional area to ascending tube cross-sectional area to reduce the flow velocity of the working fluid in the descending tube; (2) Improving combustion efficiency and regularly cleaning the surface of the tubes; (3) Paying attention to monitoring pressure changes.

VI. CONCLUSION

This study begins with heat transfer simulation to model the different heating conditions of the evaporator tube bundle in a boiler evaporation model. By simulating scenarios where each tube is uniformly heated and then analyzing the flow patterns and heat transfer conditions of each tube in an abnormal situation involving a three-tube evaporator bundle, this paper aims to provide insights. Ultimately, it is concluded that there are various reasons

for the decline in working fluid in evaporator tubes, with one significant cause being the uneven heating among the evaporator tube bundles. For a simple cycle composed of a single evaporator tube, the system is highly stable, and the two-phase flow patterns align with existing boiling conclusions. However, as the number of tubes in the bundle increases, the decline in evaporator tube performance becomes more pronounced. The uneven pressure not only leads to a decline in evaporator tube performance but also causes gases to descend in the downcomer. The primary methods to prevent such situations include reducing abnormal heating of the evaporator tubes, optimizing heat transfer, ensuring adequate combustion in the boiler, regularly maintaining the pipelines, or reducing the resistance in the downcomer.

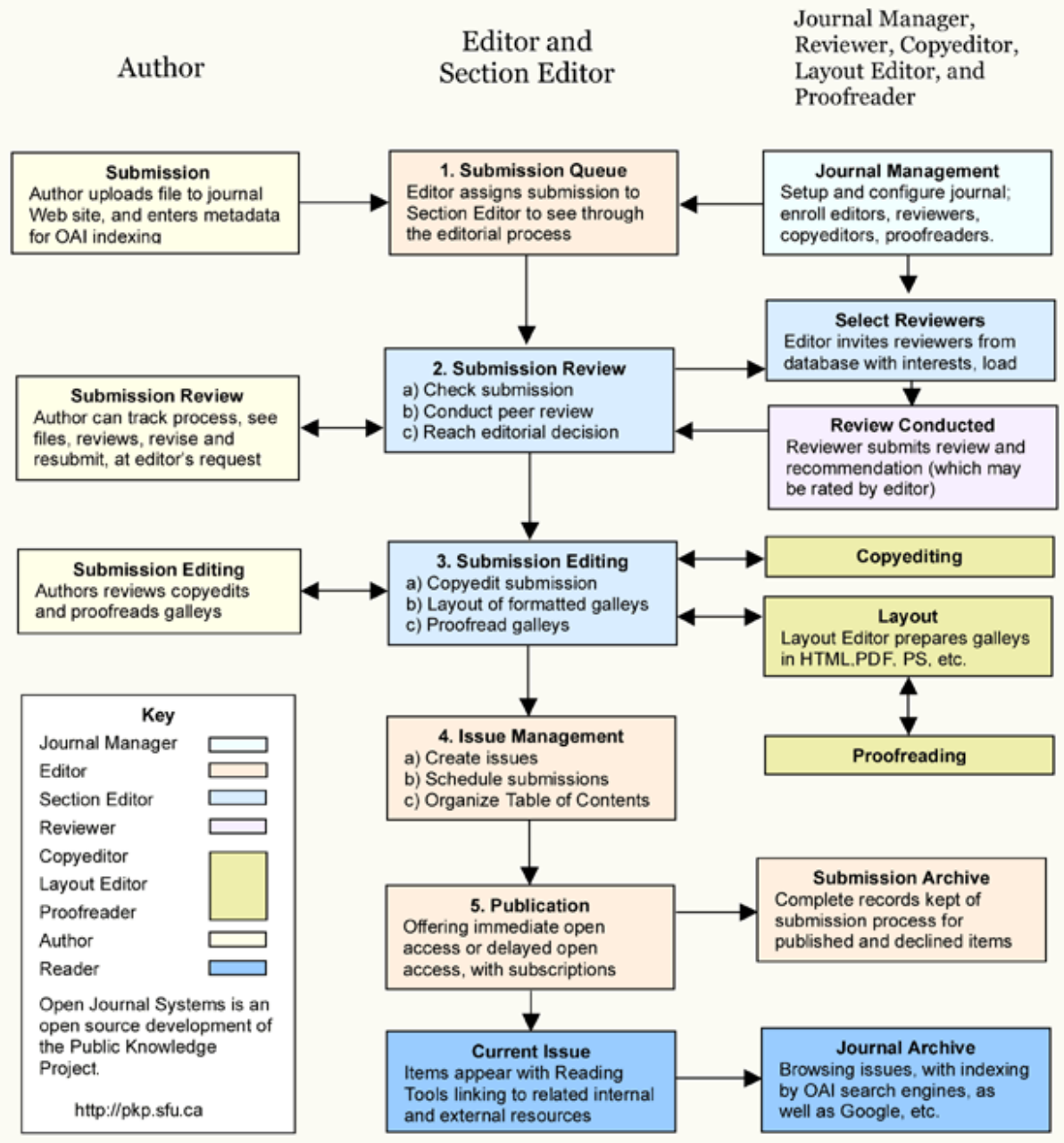
ACKNOWLEDGEMENTS

This work described in this paper was supported by the Research Funding of GDUPT, Research on Lagrangian Coherent Structure Analysis of Heat Sink for heat transfer performance with Piezoelectric Fan, Special Project of Taishi Excellent Training Plan in 2024. Special Project of Science and Technology Innovation Strategy of Guangdong Provincial Department of Science and Technology in 2024, (Project No.: 2024A0505050022).

REFERENCES

- [1] Angui Li & Xiangguo Fan. (2006). Numerical simulation prediction of natural convective heat transfer coefficient of louvered blade inclined channel under variable condition. *Journal of Xi'an University of Architecture and Technology (Natural Science Edition)* (02), 269-274+284.
- [2] Piotr Dzierwa, Dawid Taler, Marcin Trojan & Jan Taler. (2018). Optimum Heating of Boiler Evaporator. *Heat Transfer Engineering* (13-14), 1217-1226.
- [3] Guoli Tang, Junping Gu, Yuxin Wu, Zhouhang Li, Junfu Lv & Qing Liu. (2018). Flow pressure drop characteristics and defined mass flow velocity in a uniformly heated vertical riser. *Journal of Tsinghua University (Natural Science Edition)* (11).
- [4] Jia Ning. (2009). Study on the fouling characteristics of brine on enhanced heat exchange surface (Master's thesis, Dalian University of Technology).
- [5] Zhenhua Hao. (2007). Study on Hydrodynamic Characteristics of Marine Booster Boiler (Master's Thesis, Harbin Institute of Technology).
- [6] Yudong Li. (2015). Research on online vaporization technology of low-temperature medium (Master's thesis, National University of Defense Technology).
- [7] Yong Yang, Guying Yu, Fuxiang Zhang, Meng Yu & Caiguang Zhu. (2011). Study on hydrodynamic and heat transfer characteristics of supercritical pressure inclined fluorescent tubes. *Journal of Power Engineering* (11), 809-816.
- [8] Hossain Md Naim, Ghosh Koushik & Manna Nirmal K.. (2023). Performance assessment of the evaporator tubes of a natural circulation boiler by different two-phase flow models. *Journal of the Brazilian Society of Mechanical Sciences and Engineering* (8),
- [9] Zhiliang Chen. (2012). Study on aerosol particle motion and heat and mass transfer in temperature field (Ph.D. dissertation, Sichuan University). Dr.
- [10] Luyao Wang. (2021). Study on two-phase flow in ventilation cavity and its drag reduction and stabilization effect (Ph.D. dissertation, Zhejiang University). Ph.D.
- [11] Li Wan, Dong Yang, Xihong Zhou, Le Dong & Juan Li. (2020). Thermal-Hydraulic Calculation and Analysis on Evaporator System of a 1000 MW Ultra-Supercritical Pulverized Combustion Boiler with Double Reheat. *Journal of Thermal Science (prepublish)*, 1-10.
- [12] Mengyu Diao. (2018). Modeling and heat transfer analysis of vertical tube falling film evaporator (Master's thesis, Hebei University).
- [13] Zhiguang Sun. (2013). Study on the flow of falling film and the evaporative heat transfer performance of falling film in the tube (Master's thesis, East China University of Science and Technology).
- [14] Xianshi Fang, Qiuying Li, Jie Chen, Guodong Qiu & Weihua Cai. (2022). Research status and development of gas-liquid two-phase flow pattern in pipes. *Journal of Northeast Electric Power University* (04), 1-7. doi:10.19718/j.issn.1005-2992.2022-04-0001-07.
- [15] Xianshi Fang, Qiuying Li, Jie Chen, Guodong Qiu & Weihua Cai. (2022). Research status of gas-liquid two-phase flow heat transfer correlation in tubes. *Journal of Northeast Electric Power University* (01), 71-78. doi:10.19718/j.issn.1005-2992.2022-01-0071-10.
- [16] Zongyao Hu. (2023). Numerical simulation study on single-phase heat transfer enhancement of rectangular eddy current generator in tube (Master's thesis, Zhengzhou University of Light Industry).
- [17] Chao Zhang. (2022). Thermal stress analysis of vertical tube screen water wall of supercritical DC boiler. *Guangdong Electric Power* (07), 133-140.

OJS Editorial and Publishing Process



~JJAERS Workflow~

Important links:

Paper Submission Link:

<https://ijaers.com/submit-paper/>

Editorial Team:

<https://ijaers.com/editorial-board/>

Peer Review Process:

<https://ijaers.com/peer-review-process/>

Publication Ethics:

<https://ijaers.com/publication-ethics-and-publication-malpractice-statement/>

Author Guidelines:

<https://ijaers.com/instruction-to-author/>

Reviewer Guidelines:

<https://ijaers.com/review-guidelines/>

Journal Indexed and Abstracted in:

- Qualis-CAPES (A2)-Brazil
- Normatiza (Under Review- Ref.020191511)
- NAAS Score: 3.18
- Bielefeld Academic Search Engine(BASE)
- Aalborg University Library (Denmark)
- WorldCat: The World's Largest Library Catalog
- Semantic Scholar
- J-Gate
- Open J-Gate
- CORE-The world's largest collection of open access research papers
- JURN
- Microsoft Academic Search
- Google Scholar
- Kopernio - powered by Web of Science
- Pol-Index
- PBN(Polish Scholarly Bibliography) Nauka Polaska
- Scilit, MDPI AG (Basel, Switzerland)
- Tyndale University College & Seminary
- Indiana Library WorldCat
- CrossRef DOI-10.22161/ijaers
- Neliti - Indonesia's Research Repository
- Journal TOC
- WIKI-CFP
- Scinapse- Academic Search Engine
- Mendeley-Reference Management Software & Researcher Network
- Dimensions.ai: Re-imagining discovery and access to research
- Index Copernicus Value(ICV): 81.49
- Citeseerx
- Massachusetts Institute of Technology (USA)
- Simpson University (USA)
- University of Louisville (USA)
- Biola University (USA)
- IE Library (Spain)
- Mount Saint Vincent University Library (Halifax, Nova Scotia Canada)
- University Of Arizona (USA)
- INDIANA UNIVERSITY-PURDUE UNIVERSITY INDIANAPOLIS (USA)
- Roderic Bowen Library and Archives (United Kingdom)
- University Library of Skövde (Sweden)
- Indiana University East (campuslibrary (USA))
- Tilburg University (The Netherlands)
- Williams College (USA)
- University of Connecticut (USA)
- Brandeis University (USA)
- Tufts University (USA)
- Boston University (USA)
- McGill University (Canada)
- Northeastern University (USA)
- BibSonomy-The blue social bookmark and publication sharing system
- Slide Share
- Academia
- Archive
- Scribd
- ISRJIF
- Cite Factor
- SJIF-InnoSpace
- ISSUU
- Research Bib
- infobaseindex
- I2OR
- DRJI journal-repository



AI Publication

International Journal of Advanced Engineering Research and Science (IJAERS)

104/108, Sector-10, Pratap Nagar, Jaipur, India